Development of conic shell cavity

Ching-Fang Chen

Institute of Physics, Academia Sinica (ASIoP)

Frontiers in Axion Haloscope Experiment

September 3, 2026



Taiwan Axion Search Experiment with a Haloscope

- **2 - 3 GHz**
  (Cylindrical cavity)
  - 2.0 – 2.3 GHz
    - 6T: CDT045 (Dec. 2025)
    - 9T: Ongoing
  - 2.3 – 2.6 GHz
    - Undergoing Cu-coating
- **~ 5 GHz**
  - Cylindrical cavity
    - CD102 (Oct. 2021) [1], [2], [3]
  - Conic shell cavity
    - – My master's thesis
    - Cryo meas TBD

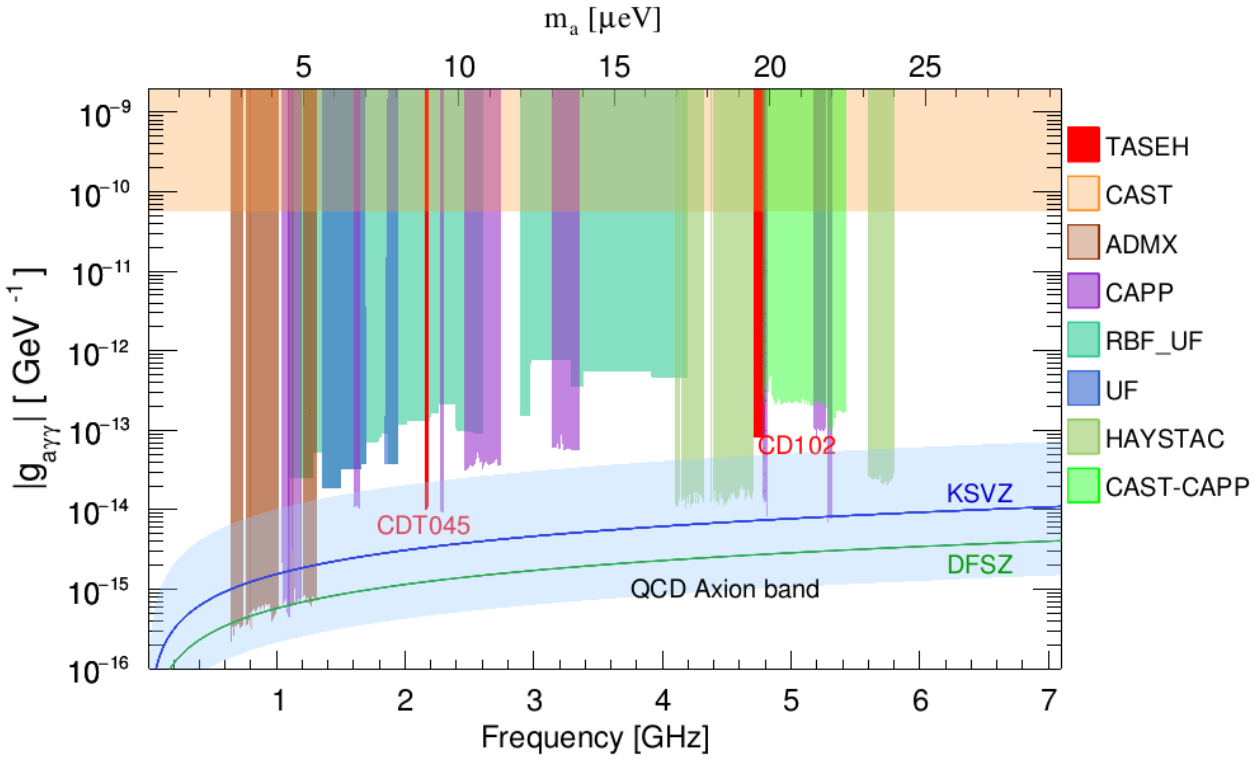


Figure 1: Axion Exclusion Plot.

Table 1: Comparison between CD102 & CDT045

	CD102	**CDT045**
B (T)	8	6
m_a (μeV)	19.47 – 19.84	8.93 – 9.01
f_r (GHz)	4.71 – 4.80	2.16 – 2.18
V (L)	0.23	4.1
C	0.62	0.46
Q_0	60000	18000
T_{sys} (K)	2.3	0.3
T_{cav} (mK)	155	162
$g_{a\gamma\gamma}/g_{a\gamma\gamma}^{KSVZ}$	11	3

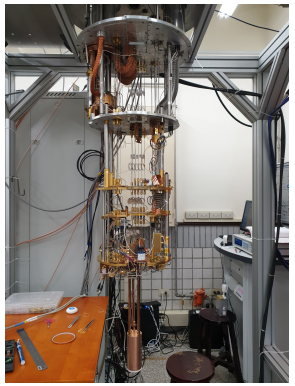


Figure 2: CD102

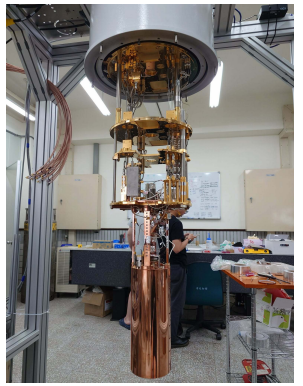


Figure 3: CDT045

Cavity Haloscope

- Fixed SNR & $\frac{df}{dt} \Rightarrow \frac{1}{g_{a\gamma\gamma}} \propto B_0 \sqrt{\frac{CV\sqrt{Q_0}}{T_{Sys}}}$
- Figure of Merit FoM = $\sqrt{CV\sqrt{Q_0}}$

C: Form factor

= Geometry factor G

$$C = \frac{\left[\int (\vec{B} \cdot \vec{E})\, dV\right]^2}{B_0^2 V \int |\vec{E}|^2\, dV} \qquad (1)$$

E: Electric field of selected mode.
B: Magnetic field of external magnet.

- Bead-pulling method

$$\Delta f \propto |\vec{E}_0|^2$$

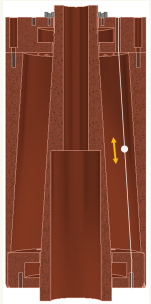


Figure 4: BP Schematic

V: Volume

- TM_{010} mode for cylindrical cavity
  - Aspect ratio ↑
    ⇒ mode density ↑
    ⇒ mode crossing ↑
  - Longitudinal symmetry break ↑
    ⇒ ACM region ↑[4]
- HF large-volume cavity design:
  - Upsize rods & radius
  - Multi-cell / Periodic structures
  - Multi-cavity configurations
  - **Advanced geometries**

Q_0: Intrinsic quality factor

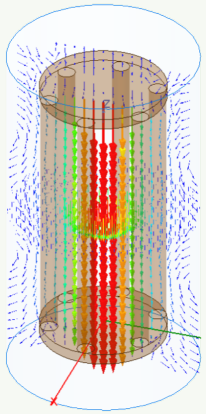
- Low T & High B environment
  - Skin depth
    - Anomalous skin depth (ASE)
  - Electron mean free path
  - Cyclotron radius

  ⇒ Non-monotonic Q_0(B, T)
- Key Factors
  - Material
    - High RRR
  - Structure
    - Split
    - 3-section: post annealing

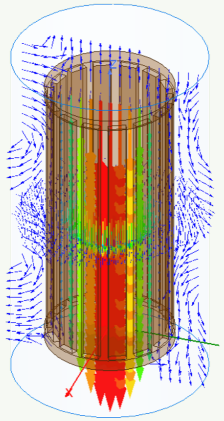
Cavities Simulation in 2021

Incomplete Wall

Q: 12973.8



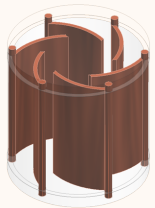
Q: 18364.8

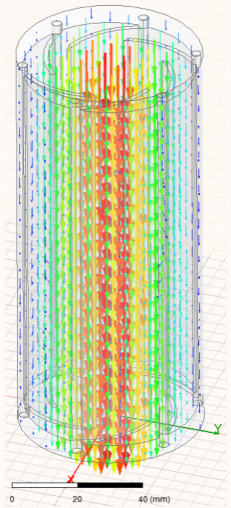


c.f. complete wall with rod
Q~20000

Aperture-like

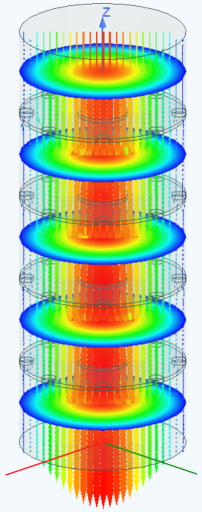
Q: 22300.1





Periodic-structure

Q: 12786.4



Multi-cell

Q: 19413

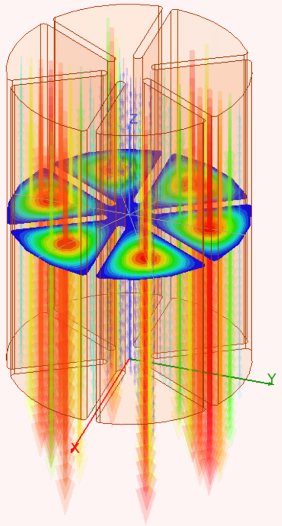


Figure 5: Cavities Simulation in 2021

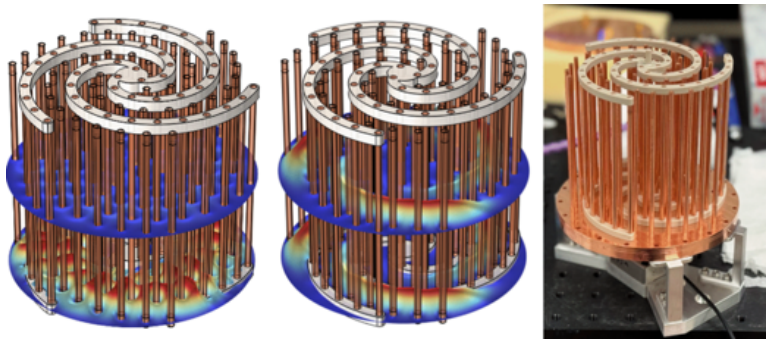


Figure 6: Spiral tuning of wire-metamaterial cavity (ALPHA) [5]

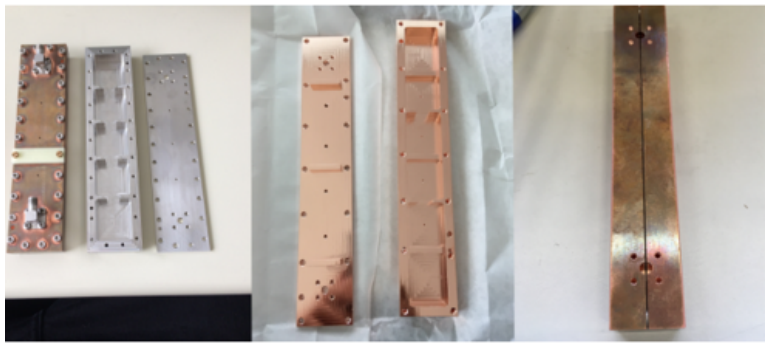
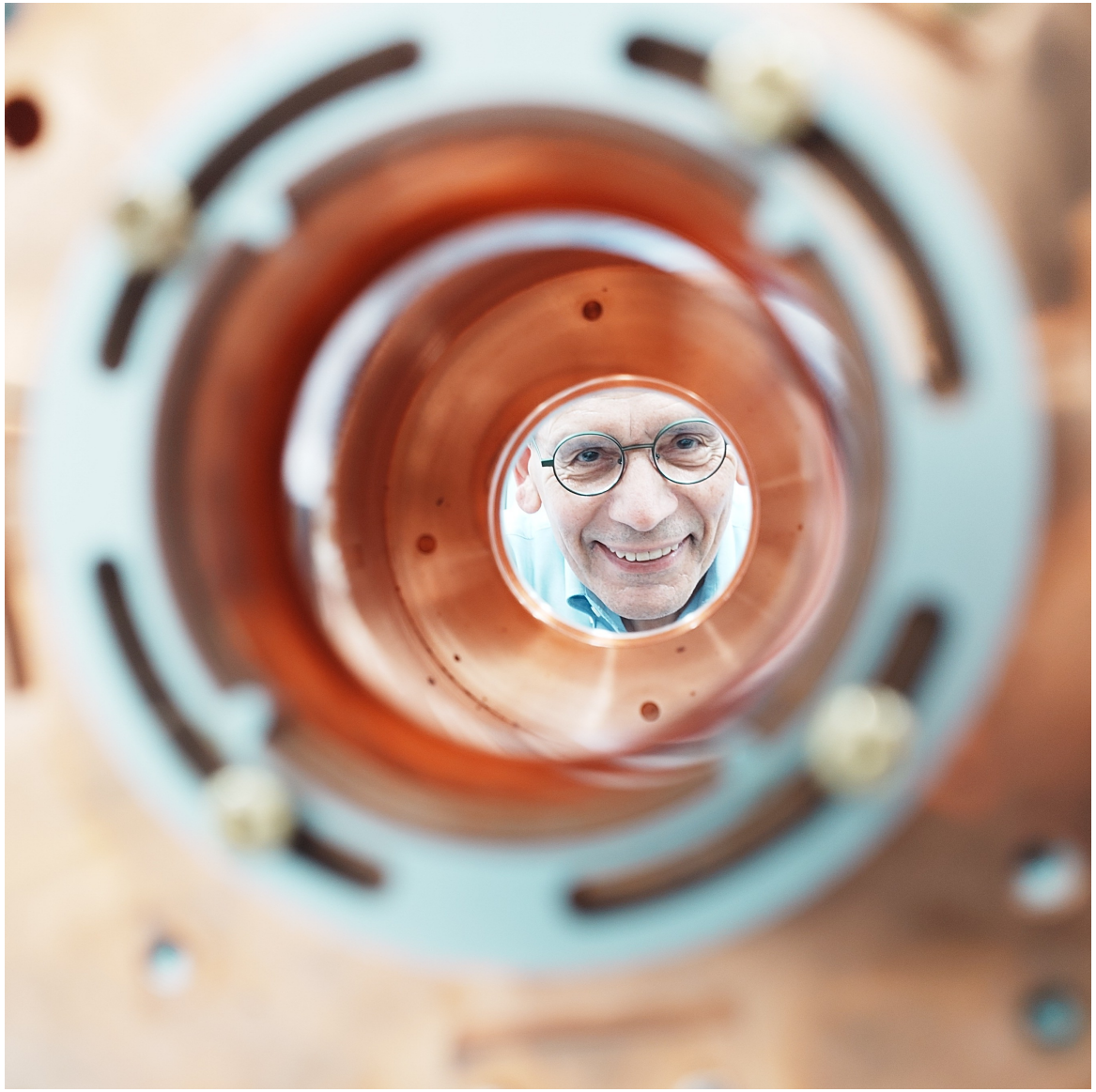


Figure 7: Cavity (RADES) [6]

Conic Shell Cavity (• ω•)





Conic Shell Cavity

- Proposed by C.L. Kuo in 2020 [7], [8]
- Large V, high C
- Two nested cones
- Frequency tuning
  - Vertically moving inner cone

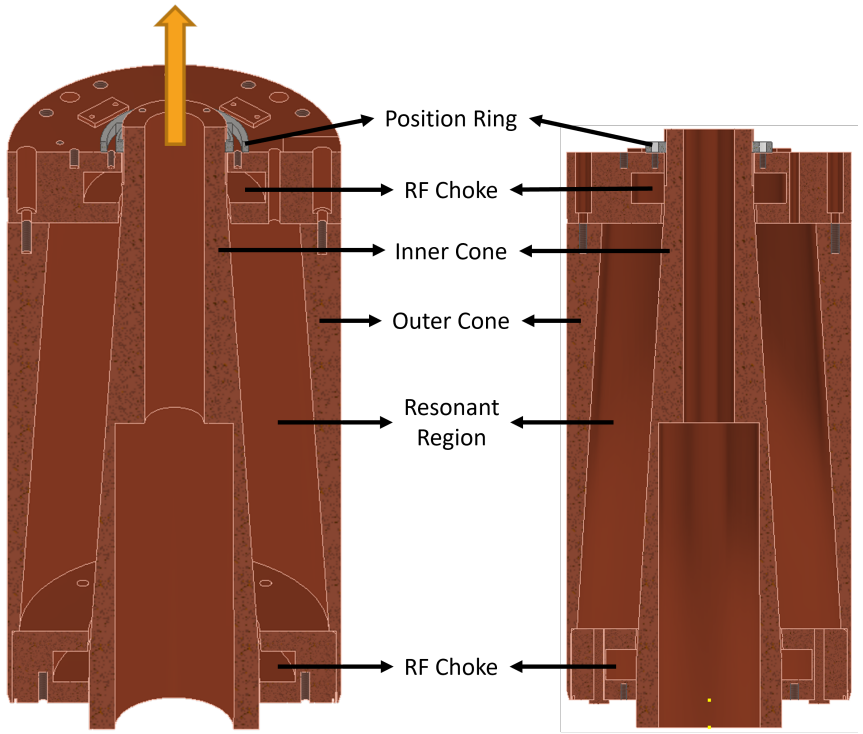


Figure 8: Conic shell cavity strucure

Theoretical Framework

- Ideal coaxial cavity
  → analytical solution
- Conic shell geometry
  → Second-order perturbative solution

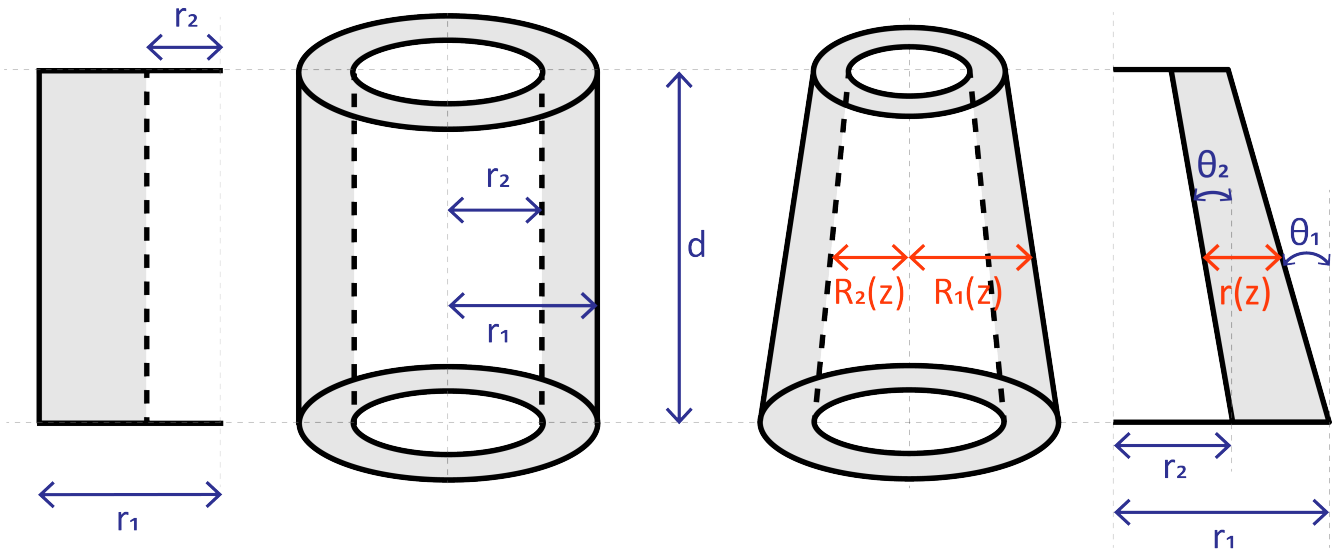


Figure 9: Theoretical Frame. (Left) Coaxial cavity; (Right) Conic shell cavity.

Theoretical Framework

- Assume $B_z = B_0 = \text{const.}$
  - Coaxial cavity
    - $r_1 = 65$ mm; $\eta = \frac{r_2}{r_1}$

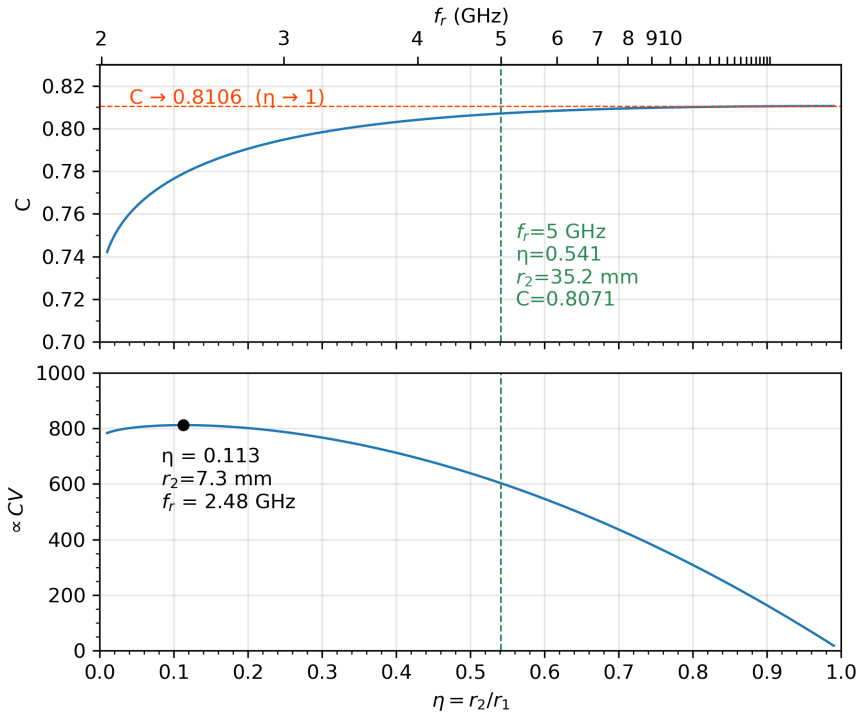


Figure 10: Optimization of C and CV

Form factor decomposition

$$C = \frac{\left(\int \vec{E}_z \, dV\right)^2}{V \int |\vec{E}_z|^2 dV} = \frac{N^2}{VP}$$

- Conic shell cavity
  - $r_1 = 65$ mm; $\eta = \frac{r_2}{r_1}$; $\theta_1 = 3.55° = ;\ \theta_2 = 3.5°$

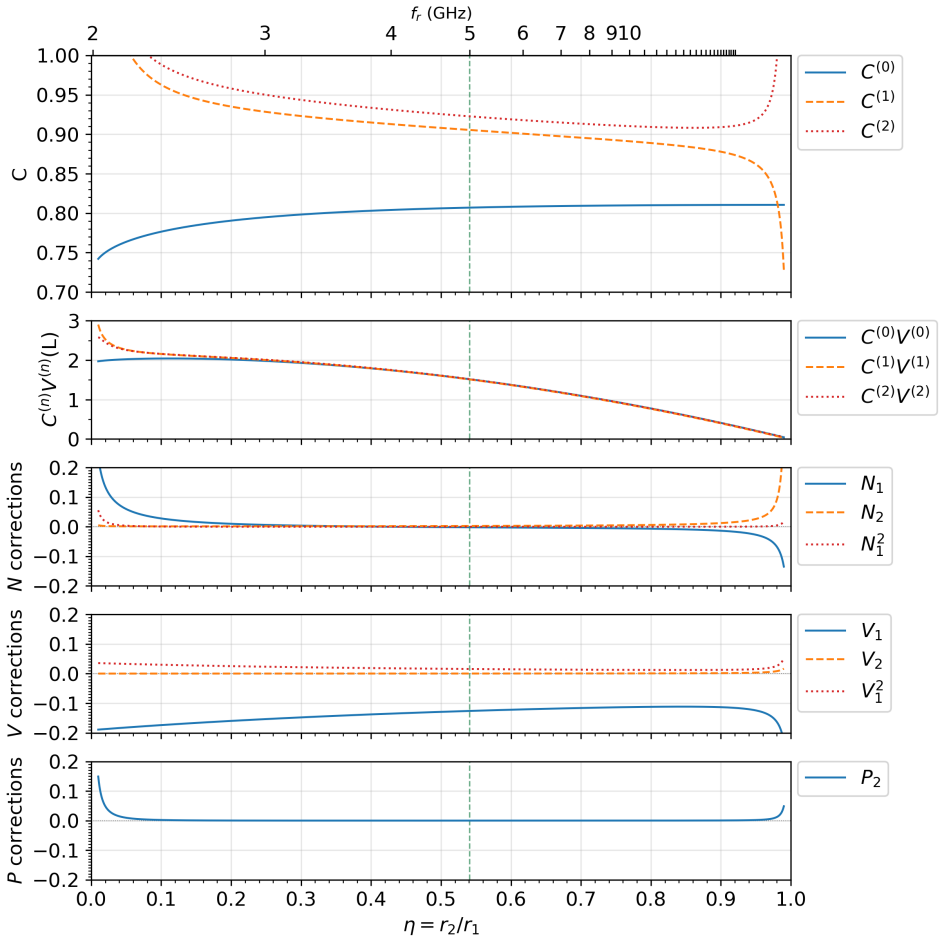


Figure 11: Perturbative corrections

Dimension (Eigenmode solver)

- θ_{In} = 3.5°
- f_r @ 5 GHz, W_0=29.98 mm
- Optimization
  - H_{out} = 200 mm
  - θ_{Out}= 3.55°
- H_{In} = 224 mm

  ⇒ Tuning range 24 mm

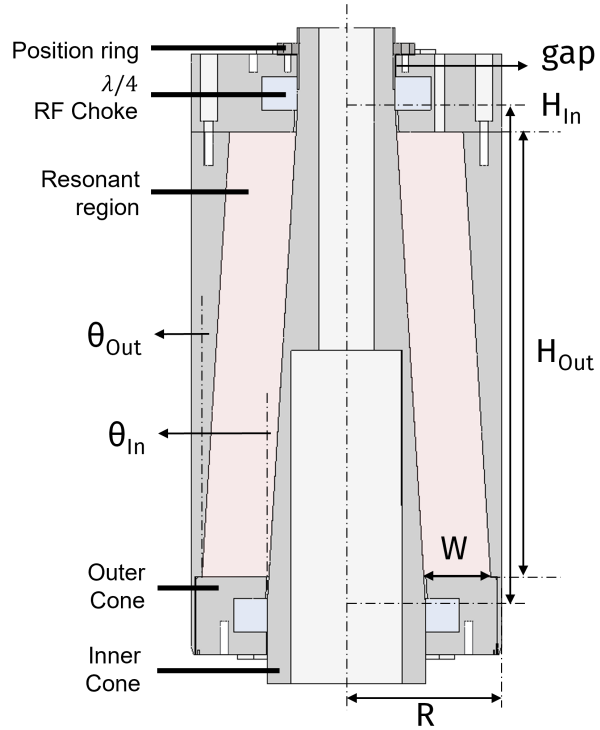


Figure 12: Dimension

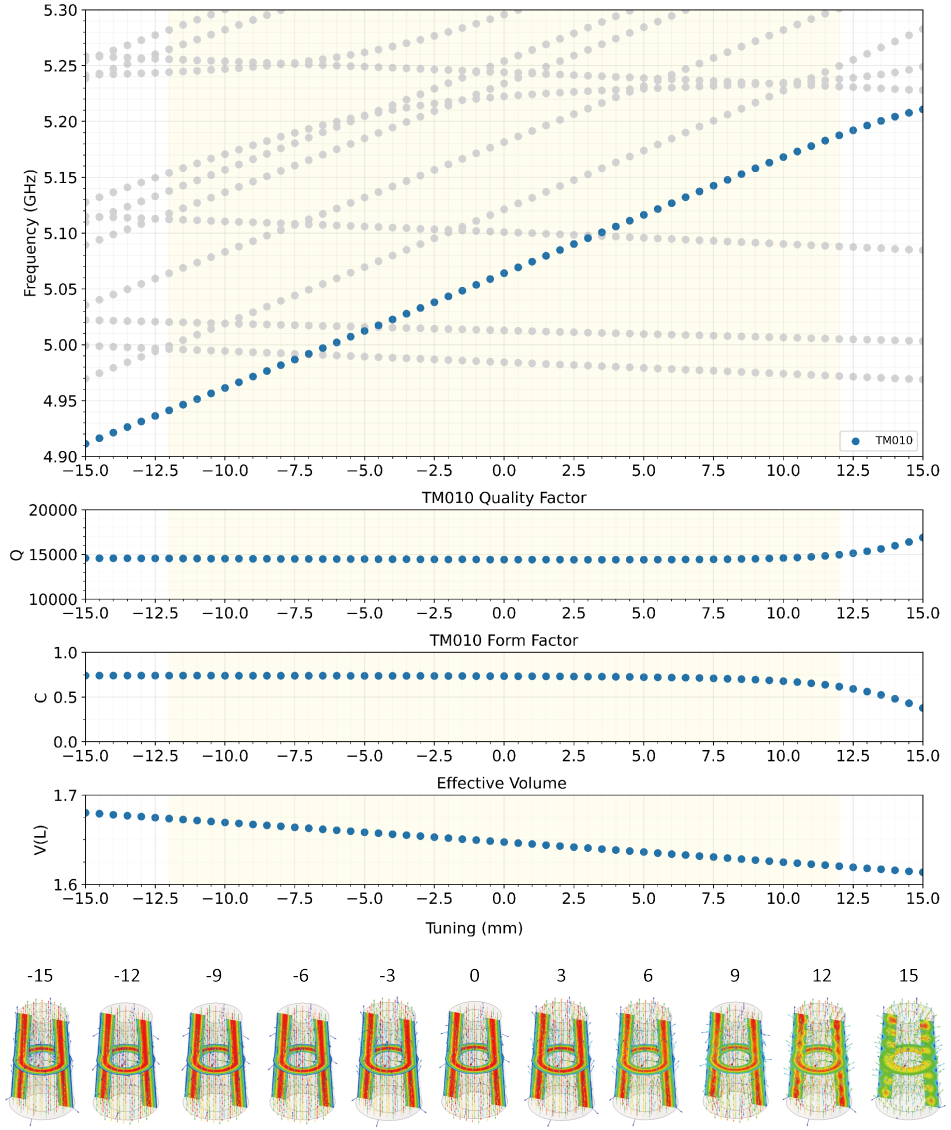


Figure 13: Eigenmode

θ_{Out} Optimization

- H_{Out} = 200 mm
- θ_{In} = 3.5°

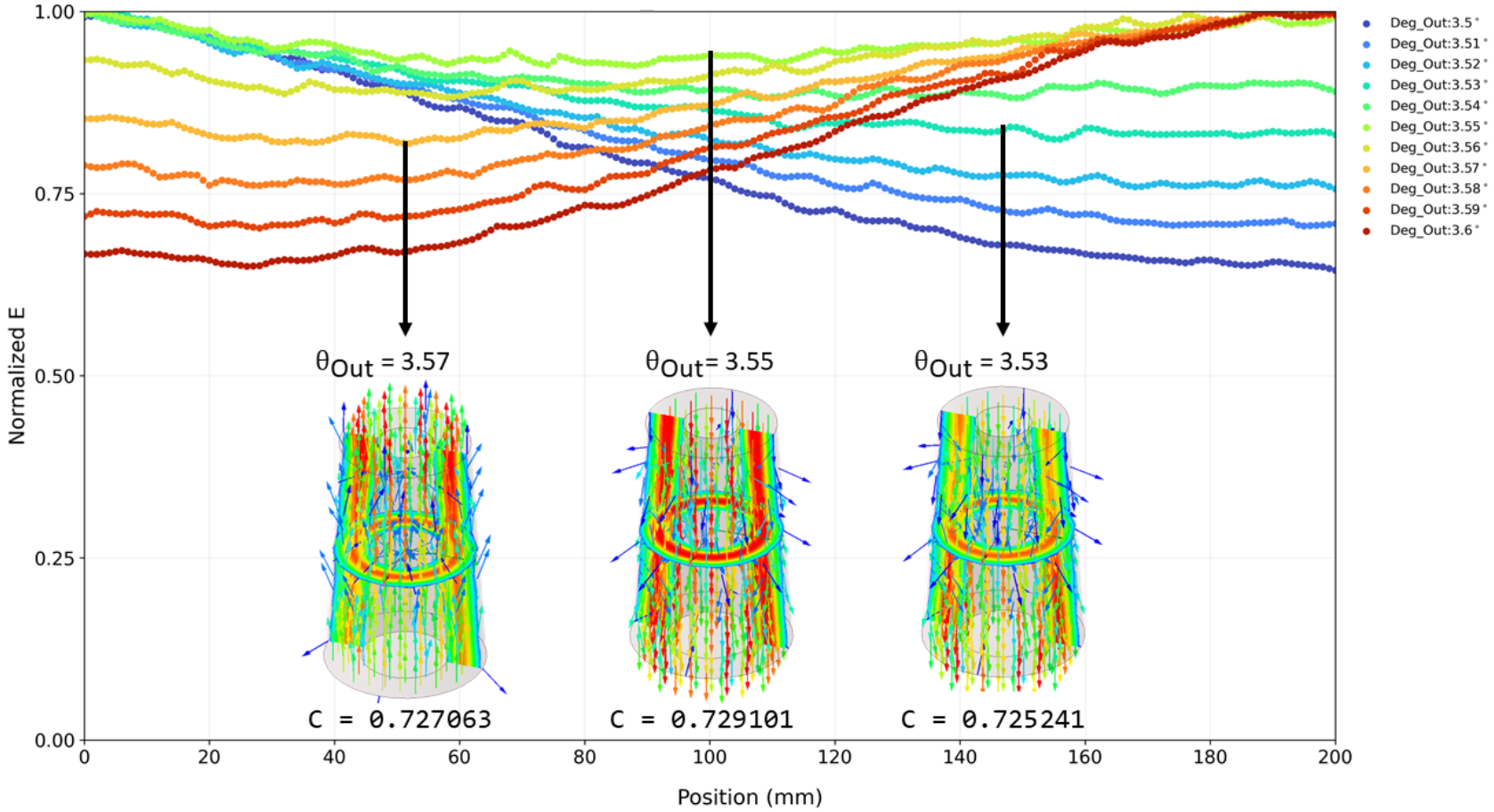


Figure 14: Normalized electric field distribution along the cavity centerline for different θ_{Out}.

FoM Comparison

Table 2: FoM comparison among axion haloscope experiments operating near 5 GHz.

Cavity	Tuning Range (GHz)	Volume (L)	Q_0 at room temp.	C	FoM
CAPP 8-Cell [9]	5.83 – 5.94	3.1	15000	0.6	15.09
Conic Shell	4.91 – 5.21	1.67	14500	0.73	**12.04**
HAYSTAC Phase I [10]	Run 1: 5.7–5.8 Run 2: 5.6–5.7	2	(LT) 30000	0.5	~11.07
HAYSTAC Phase II [11]	II(c): 4.178–4.459 II(d): 4.523–4.707	1.545	(60 mK) 44000 ± 4000	0.43 ± 0.01	~9.02
CAPP 18T [12]	4.72 – 5.06	1.07	12000 – 18000	0.56 – 0.58	8.64
ADMX Sidecar [13]	(A) 4.202–4.249 (B) 5.086 – 5.799	0.38	11000	(A) 0.49 (B) 0.44 – 0.61	4.46
TASEH CD102 [1]	4.662 – 4.951	0.234	18000	0.62	4.41
CAST-CAPP [14]	4.774 – 5.434	0.224	~10000	0.53 ± 0.05	~3.45

- CAST-CAPP: Multi-cavity
- CAPP 8-Cell: Multi-cell cavity

Mode Map (Driven Modal solver)

- $f_{r_{TM_{010}}}$: 4.94575 – 5.18875 GHz
- Tuning rate: 10.125 MHz/mm
- Q_0 ~ 13350

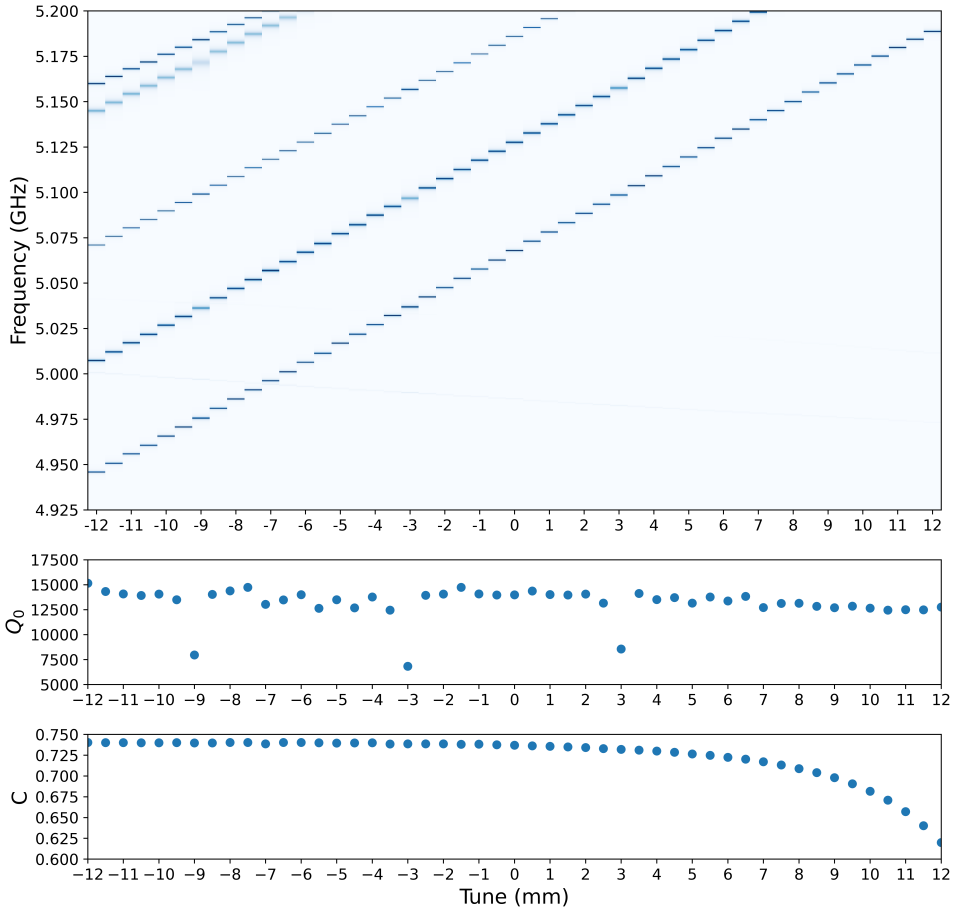


Figure 15: Mode map

- Misalignment simulation
  - Shift
  - Rotation

⇒ Once TM_{010} mode is excited, C > 0.7222 (tune=0)

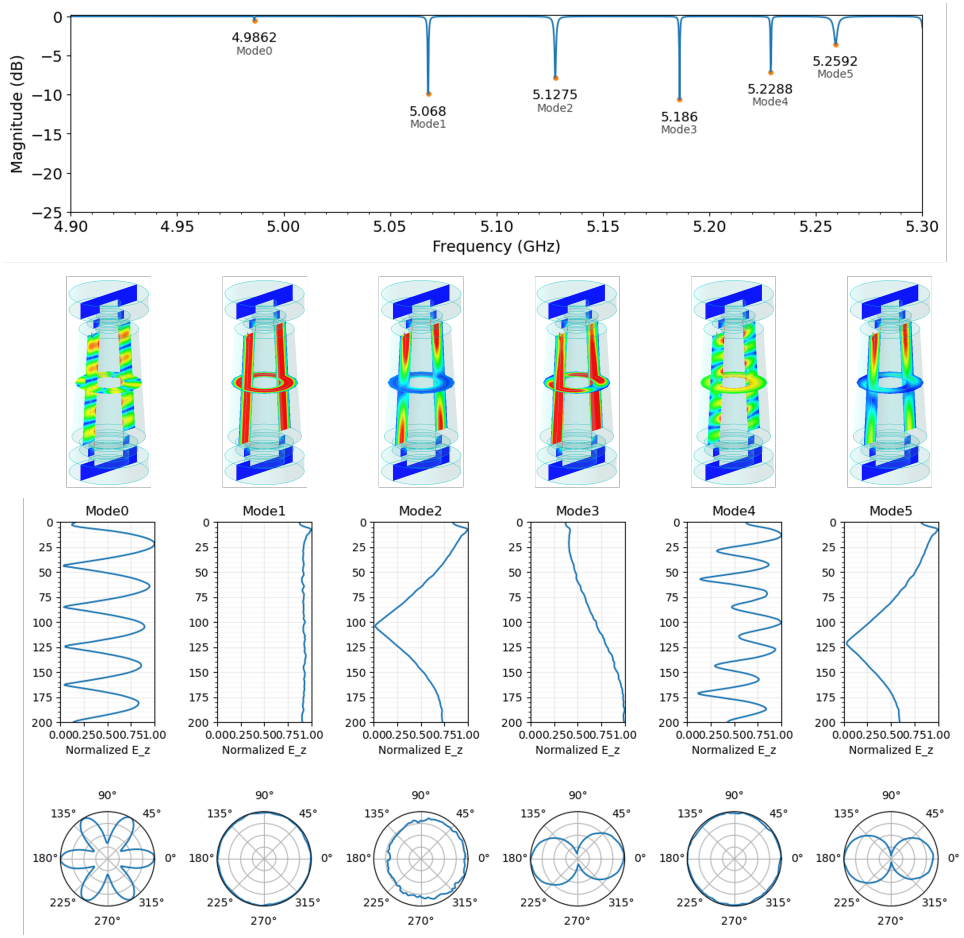


Figure 16: *S* parameter & E-field at Tune = 0 mm

Misalignment

- Shift schematic

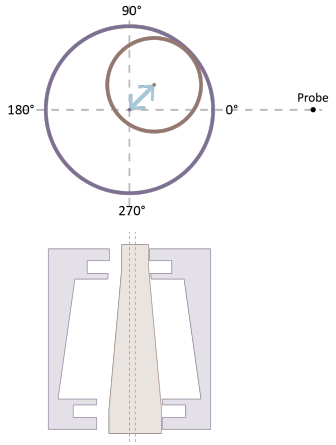


Figure 17: Shift schematic

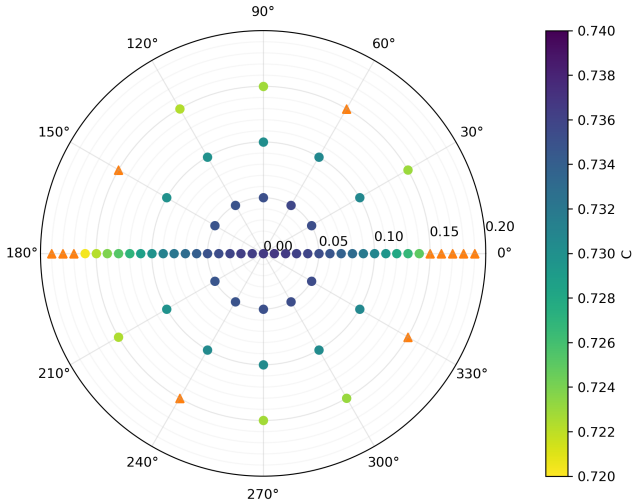


Figure 18: Shift misalignment simulation

- Rotation

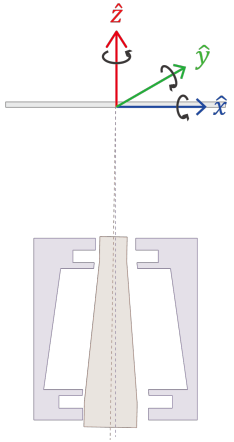


Figure 19: Rotation schematic

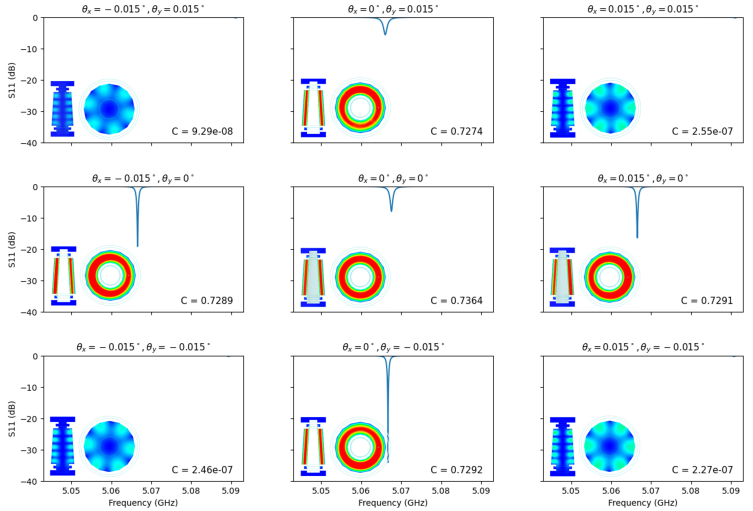


Figure 20: Rotation misalignment simulation

- TM_{010} mode excited → $C > 0.722$ (c.f. without misaligment 0.7366)

Fabrication

Cavity Structure: S.S.316 + Cu Coating

- Machining & 3D Measurement
  - Three sections & No fillet
    → Precise angle
  - Positioning ring
    → Mechanical alignment
  - Argon welding
    → Sealing with minimal deformation

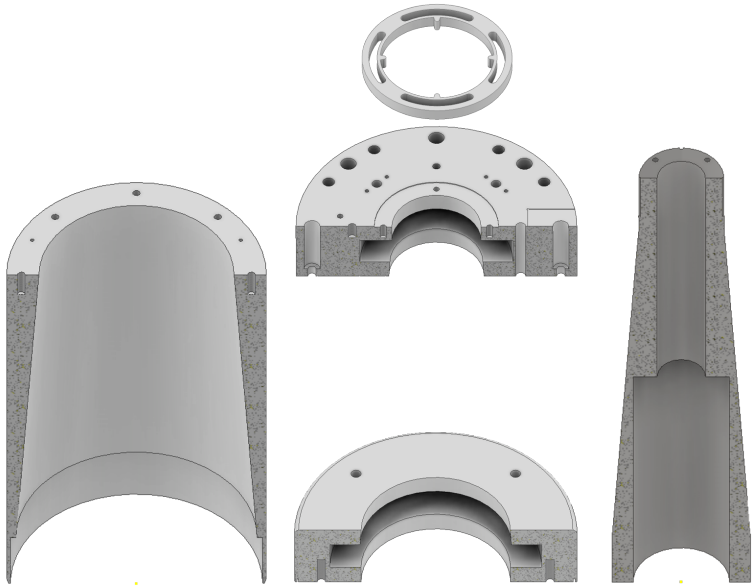


Figure 21: Machining

- Copper coating
  - Cu: 2 hrs
  - Ag-strike, Ni-strike: enhance adhesion
  - SS316: substrate

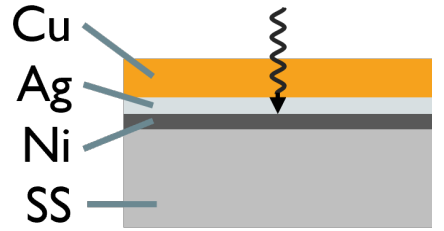


Figure 22: Coating Procedure

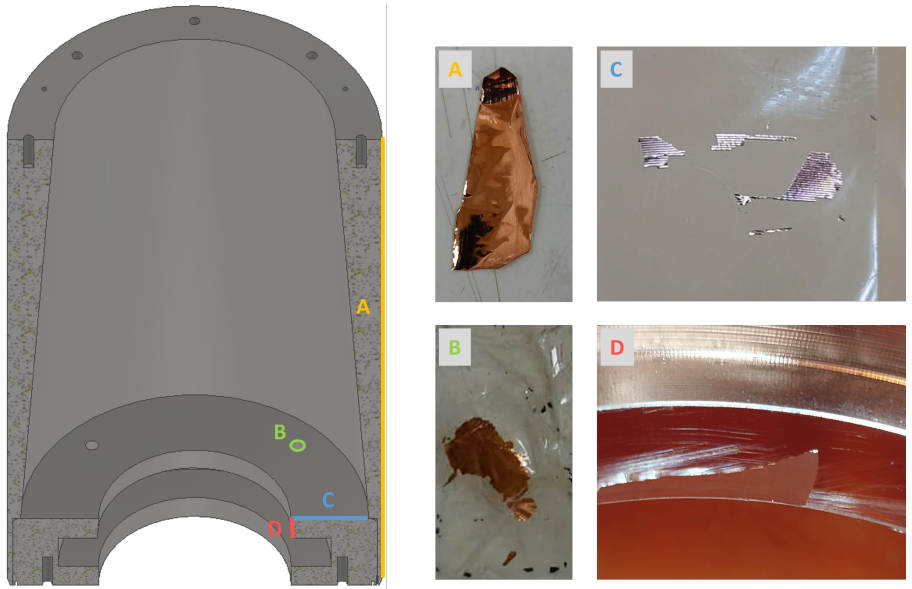


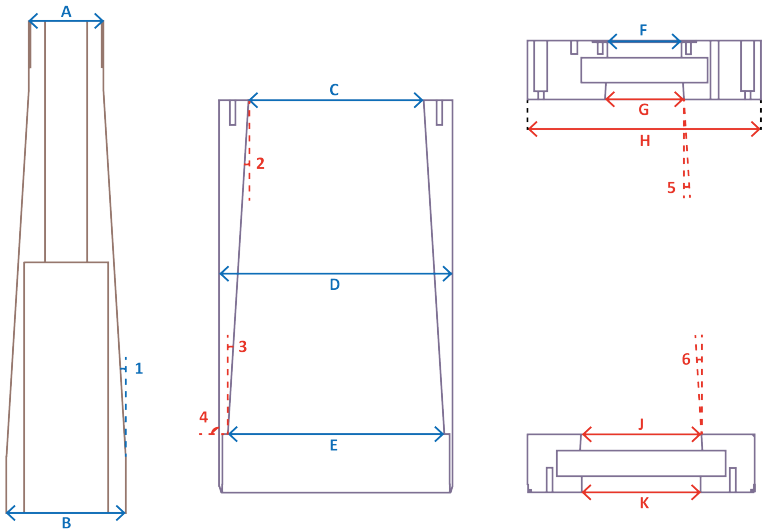
Figure 23: The peeled-off coating thickness:(A) Cu: 50–60 μm, (B) Cu: 7 μm, (C) Cu: 2.33 μm; Ni: 0.03 μm, (D) Cu: 16 μm.

3D Measurement

Table 3: 3D Measurement Result

Label	Designed (mm)	Measured (mm)	Eccentricity (mm)
A	44.10	44.119	0.005
B	71.50	71.564	0.005
C	105.18	105.222	0.119
D	140.00	140.054	0.012
E	130.00	130.049	0.076
F	44.50	44.507	0.005
G	47.56	47.538	0.003
H	140.00	139.958	0.023
J	71.78	71.772	0.016
K	71.90	71.899	0.015

Label	Designed (deg)	Measured (deg)
1	3.50	3.517
2	3.55	3.521 / 3.552
3	3.55	3.549 / 3.570
4	90	/ 89.986
5	3.50	3.469
6	3.50	3.452



Experimental Setup

- Room Temperature

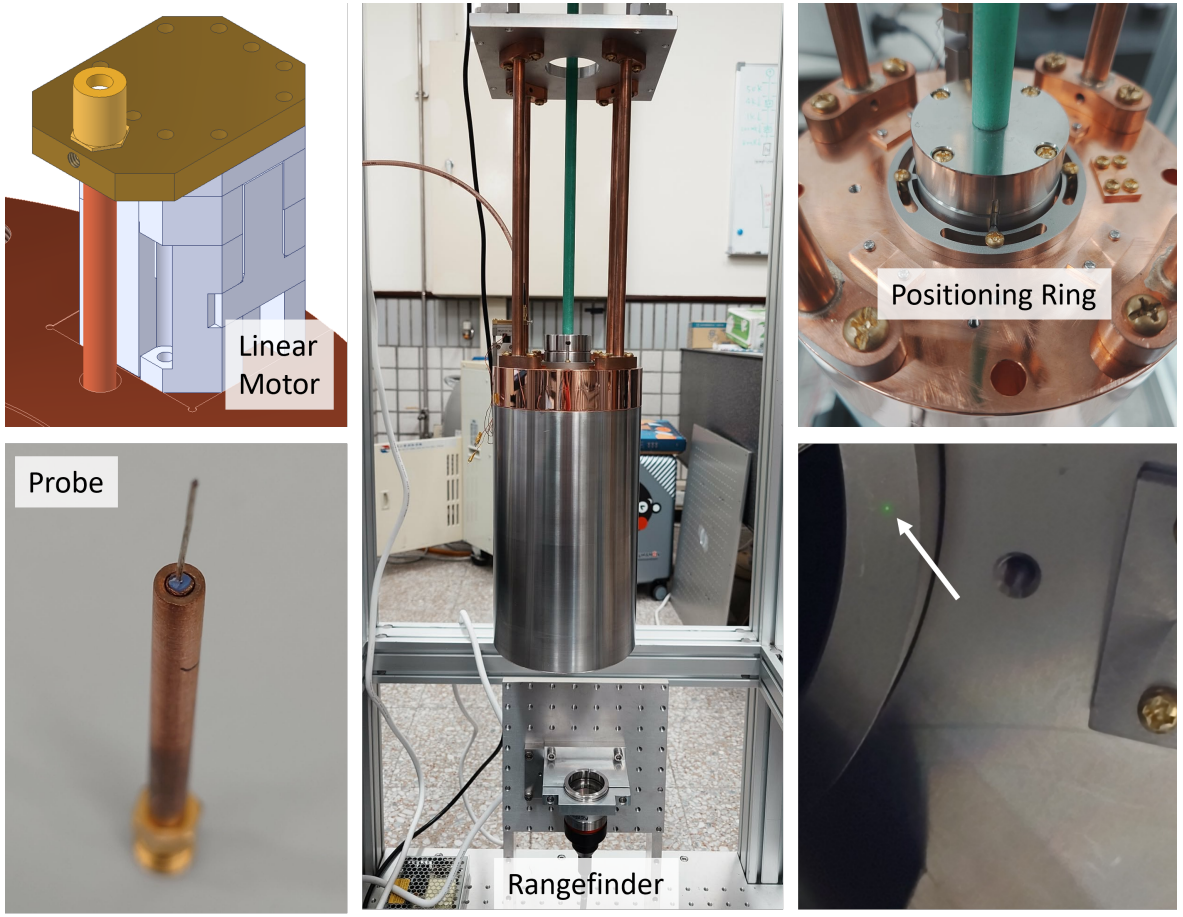


Figure 24: RT Setup

- Cryogenic

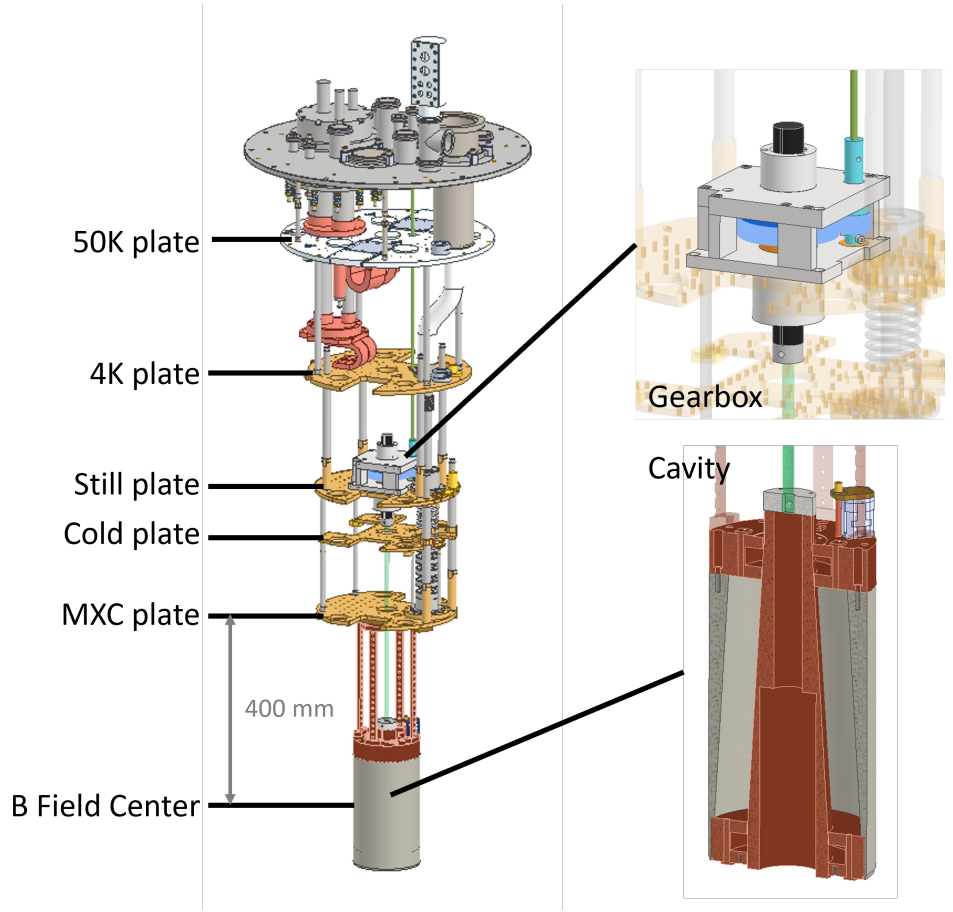


Figure 25: LT Setup

- Probe: Jyebao ".085CU-W-P-50" semi-rigid coaxial cable + "SMA8300-0085" SMA jack
- Coupling tuning: Attocube ANPz101eXT12/RT linear z-axis nanopositioner
- Frequency tuning: high-torque motor ↔ G-10 rod ↔ inner cone

Ideas for Future Research

- Integrate conical shell cavities with ULC and auxetic structures
  - ULC → Reduce cavity weight
    - Reduce cavity mass
    - Use OFHC copper or HTS → eliminate the need for coating
  - Auxetic structure
    - Divide the inner cone into several strips and adjust their positions

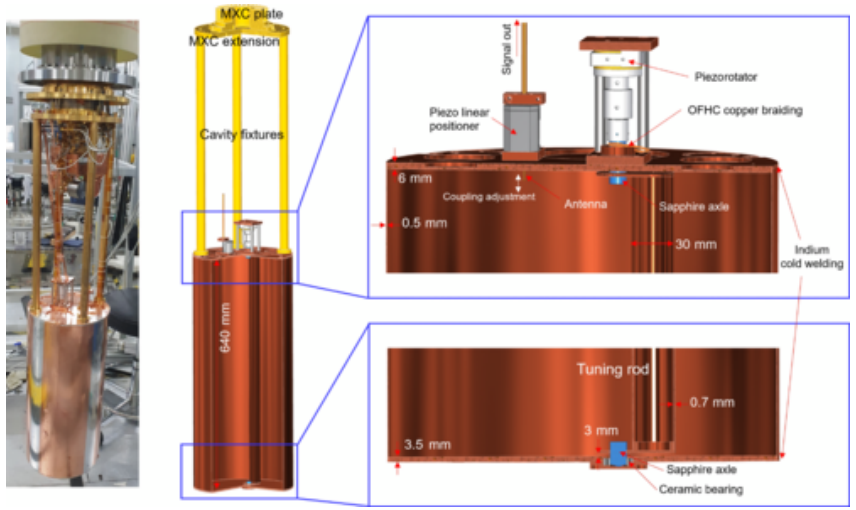


Figure 26: ULC (CAPP) [15]

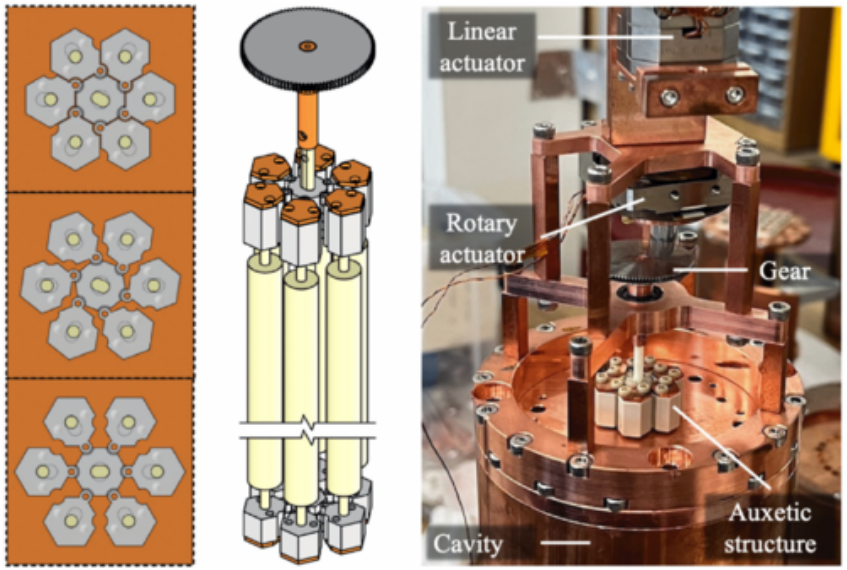
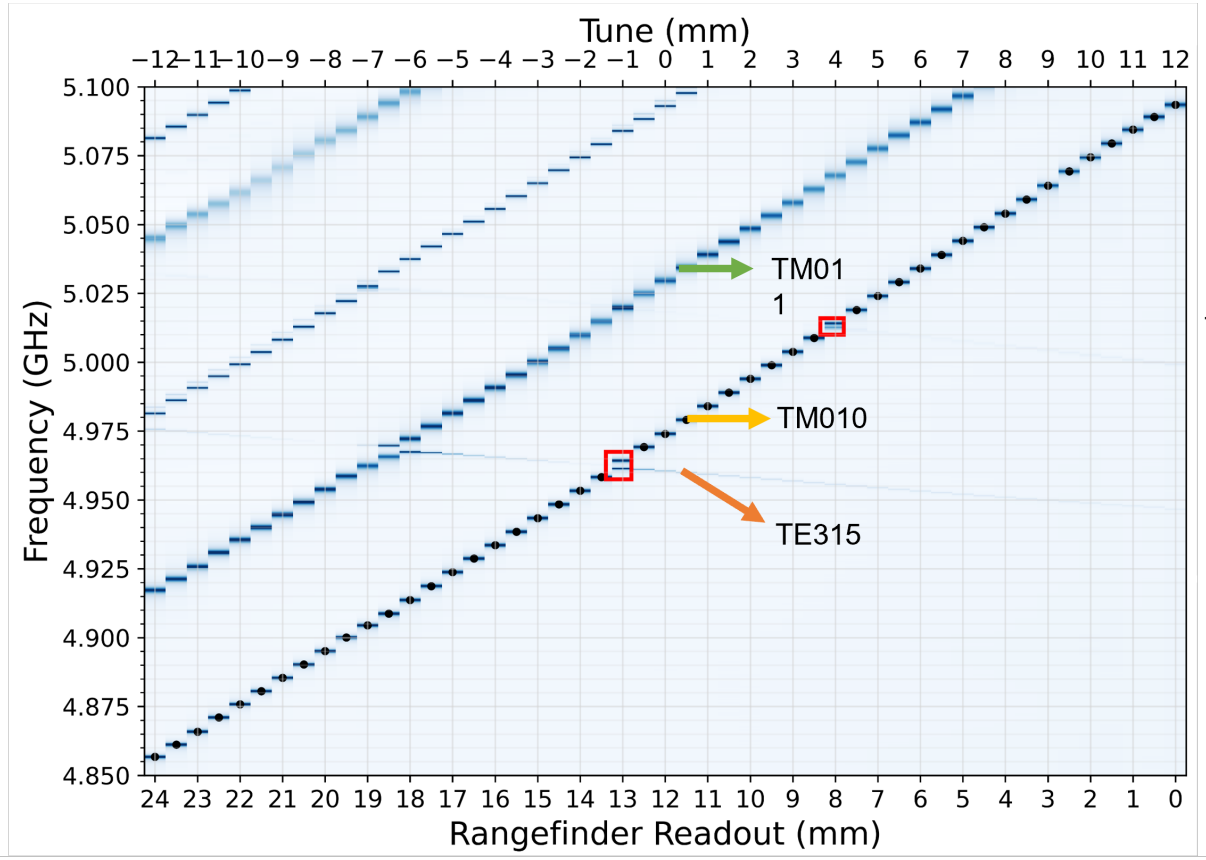
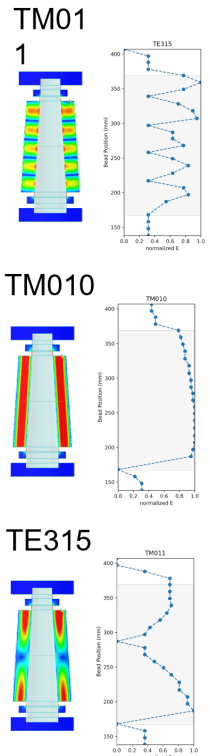


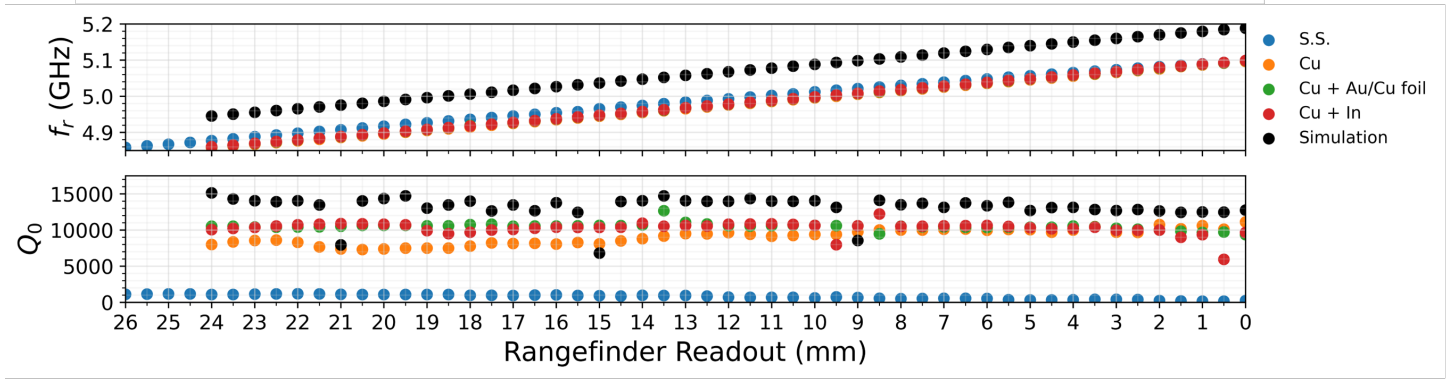
Figure 27: Auxetic structure (CAPP) [16]

- Fix the innermost and outermost walls, sharing the middle wall
  - Form two conical shell cavities and tune both simultaneously
  - Two readouts → multicavity configuration

RT Measurement







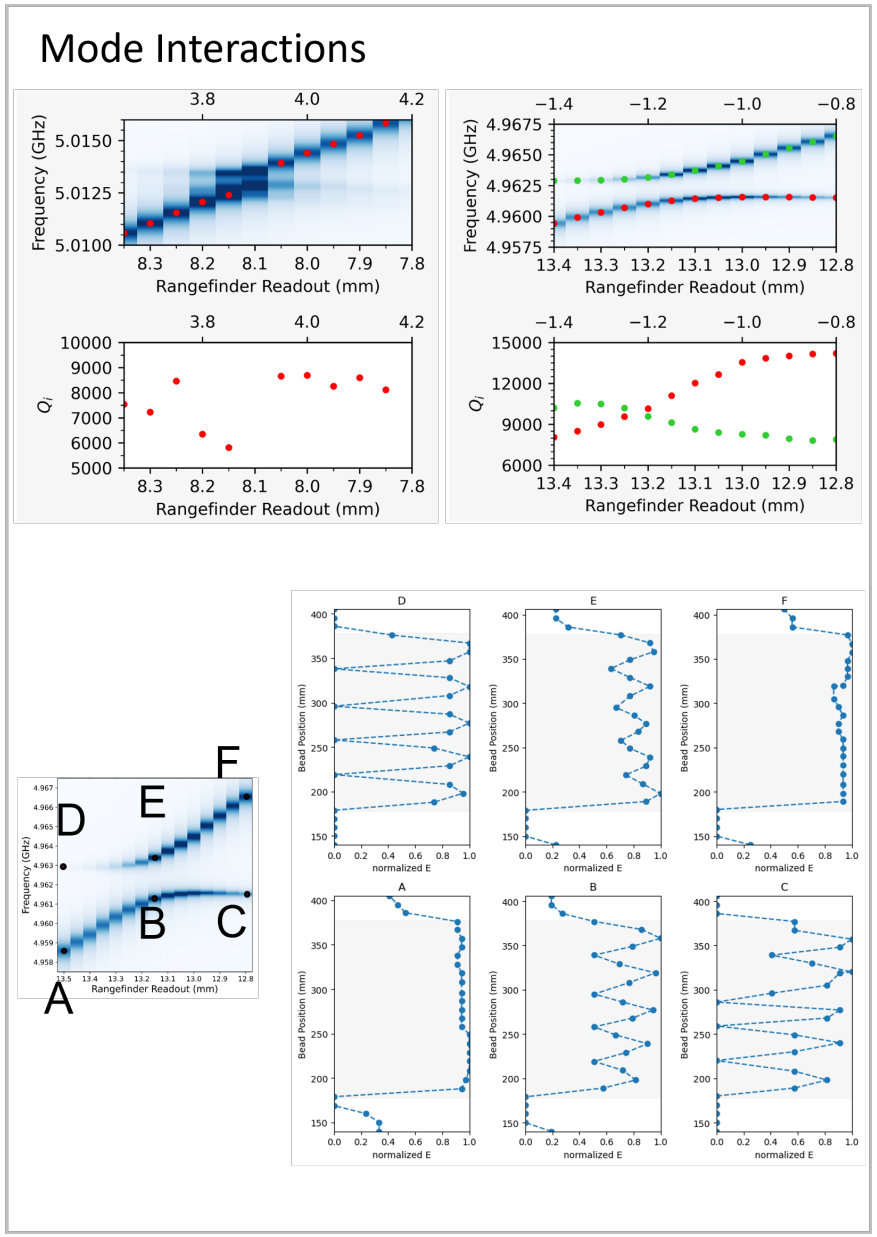


Figure 28: Room temperature measurement

Discrepancy Analysis

- After inner cone position calibration: Δf_r ~ 69.7 MHz (~ 1.39%)
- After filling Indium or Au/Cu foil at contact surface: $\frac{Q_{meas}}{Q_{sim}}$ ~ 77%
- **Refined simulation**:
  - air environment
  - layered impedance B.C.
  - measured 3D dim
- Potential factors:
  - **Simulation mesh resolution**
    - Rectilinear: Δf_r ~ 0.52%
      $\left(\frac{R_{\text{eff}}}{R} \approx 1 - \frac{\pi^2}{3N^2}\right)$
    - Curvilinear: Δf_r ~ 0.19%
  - **Surface roughness**
    - R_a = 0.45 μm: $\frac{Q_{meas}}{Q_{sim}}$ ~ 98.81%
  - Field penetration ($\mu_{r_{Ni}}$)
    - Landau–Lifshitz model [17]
  - Probe coupling effects

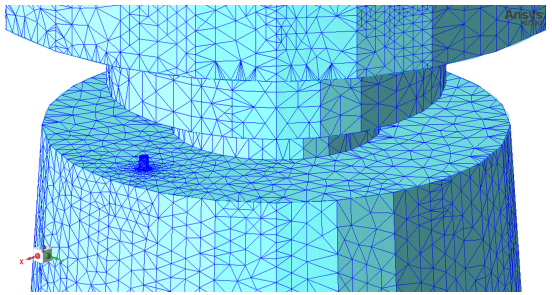


Figure 29: Rectilinear

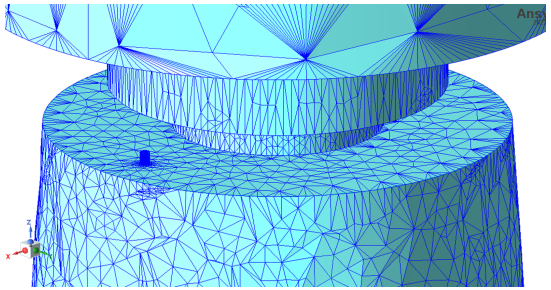


Figure 30: Curvilinear

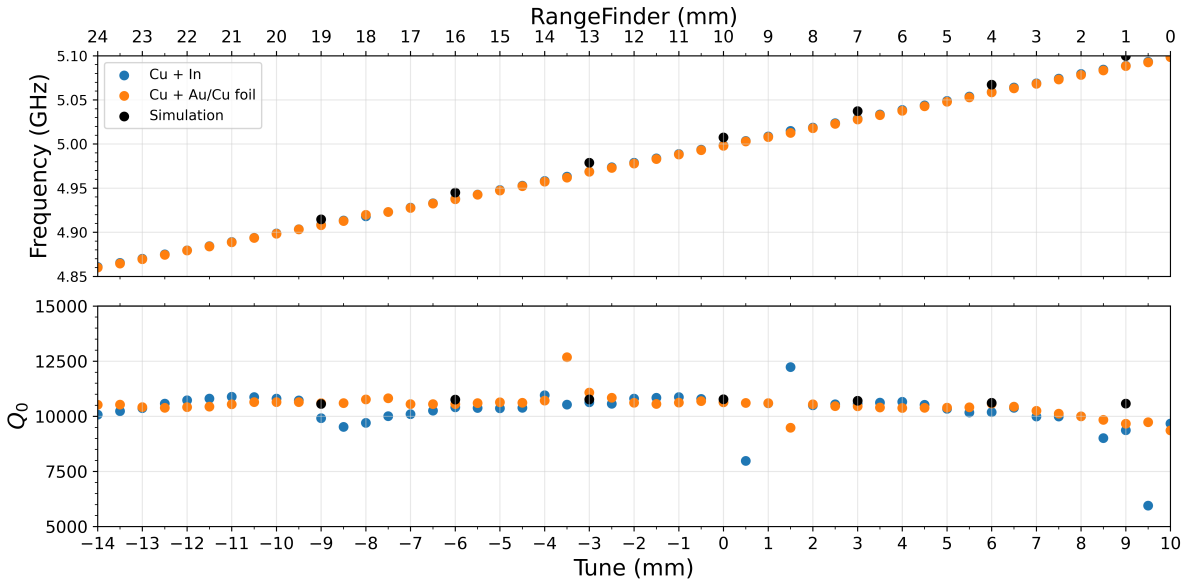
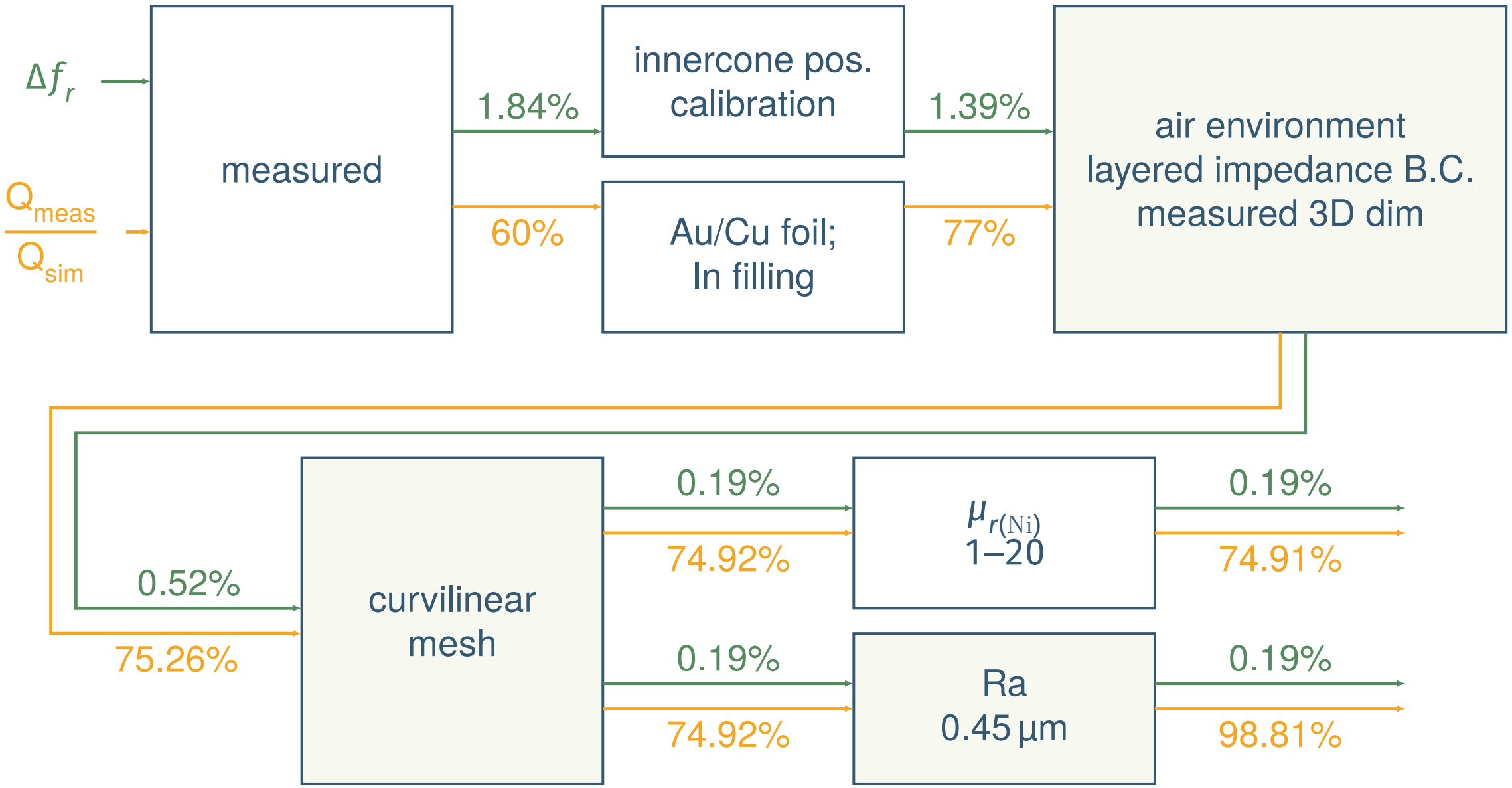


Figure 31: Comparison between meas and refined sim

Discrepancy Analysis



Summary

- Cavity properties
  - $C \approx 0.73$, $V \approx 1.67$ L, measured Q_0 (RT)$\approx$ 10,500
  - f_r: 4.859 – 5.098 GHz
  - Tuning rate: 9.94 MHz/mm
  - FoM ~2.7× that of CD102 → ~53× reduction in scan time
- Analytical coaxial model with 2nd-order perturbation
- Misalignment robust: $C > 0.722$ once TM_{010} is excited
- Refined simulation
  (curvilinear mesh, layered impedance, $\mu_{r_{Ni}}$, surface roughness R_a):
  - Δf_r : 1.84% → 0.19%
  - $\frac{Q_{meas}}{Q_{sim}}$: 77% → 98.81%
- Future works
  - Electroplating optimization → Cu thickness > 7 δ
    - Potential alternatives: electroforming / cold spray / HIP / HTS tape
  - Split outer-cone design to reduce contact resistance
  - Cryogenic + 9 T characterization

Reference

Reference I

[1] H. Chang et al., "First results from the Taiwan Axion Search Experiment with a Haloscope at 19.6 μeV," *Phys. Rev. Lett.*, vol. 129, p. 111 802, 11 Sep. 2022.

[2] H. Chang et al., "Taiwan Axion Search Experiment with Haloscope: CD102 analysis details," *Phys. Rev. D*, vol. 106, p. 052 002, 5 Sep. 2022.

[3] H. Chang et al., "Taiwan Axion Search Experiment with Haloscope: Designs and operations," *Review of Scientific Instruments*, vol. 93, no. 8, p. 084 501, Aug. 2022.

[4] I. Stern et al., "Avoided mode crossings in cylindrical microwave cavities," *Phys. Rev. Appl.*, vol. 12, p. 044 016, 4 Oct. 2019.

[5] J. Lindahl et al., "Spiral tuning of wire-metamaterial cavity for a plasma haloscope," *Phys. Rev. Appl.*, vol. 25, p. 024 073, 2 Feb. 2026.

[6] A. Á. Melcón et al., "Axion searches with microwave filters: The rades project," *Journal of Cosmology and Astroparticle Physics*, vol. 2018, no. 05, p. 040, May 2018.

[7] C.-L. Kuo, "Large-volume centimeter-wave cavities for axion searches," *Journal of Cosmology and Astroparticle Physics*, vol. 2020, no. 06, p. 010, Jun. 2020.

[8] C.-L. Kuo, "Symmetrically tuned large-volume conic shell-cavities for axion searches," *Journal of Cosmology and Astroparticle Physics*, vol. 2021, no. 02, p. 018, Feb. 2021.

[9] S. Ahn et al., "Probing Kim-Shifman-Vainshtein-Zakharov axion dark matter near 5.9 GHz using an 8-cell cavity haloscope," *Phys. Rev. Lett.*, vol. 135, p. 211 801, 21 Nov. 2025.

[10] L. Zhong et al., "Results from phase 1 of the HAYSTAC microwave cavity axion experiment," *Phys. Rev. D*, vol. 97, p. 092 001, 9 May 2018.

[11] X. Bai et al., "Dark matter axion search with HAYSTAC Phase II," *Phys. Rev. Lett.*, vol. 134, p. 151 006, 15 Apr. 2025.

[12] H. Yoon et al., "Axion haloscope using an 18 t high temperature superconducting magnet," *Phys. Rev. D*, vol. 106, p. 092 007, 9 Nov. 2022.

[13] C. Boutan et al., "Piezoelectrically tuned multimode cavity search for axion dark matter," *Phys. Rev. Lett.*, vol. 121, p. 261 302, 26 Dec. 2018.

[14] C. M. Adair et al., "Search for dark matter axions with CAST-CAPP," *Nature Communications*, vol. 13, no. 1, p. 6180, Oct. 2022.

[15] S. Ahn et al., "Extensive search for axion dark matter over 1 ghz with CAPP's main axion experiment," *Phys. Rev. X*, vol. 14, p. 031 023, 3 Aug. 2024.

[16] S. Bae et al., "Search for dark matter axions with tunable TM_{020} mode," *Phys. Rev. Lett.*, vol. 133, p. 211 803, 21 Nov. 2024.

[17] Y. Shlepnev and S. McMorrow, "Nickel characterization for interconnect analysis," in *2011 IEEE International Symposium on Electromagnetic Compatibility*, Aug. 2011, pp. 524–529.

[18] P. Sikivie, "Invisible axion search methods," *Rev. Mod. Phys.*, vol. 93, p. 015 004, 1 Feb. 2021.

[19] S. Weinberg, "A new light boson?" *Phys. Rev. Lett.*, vol. 40, pp. 223–226, 4 Jan. 1978.

[20] F. Wilczek, "Problem of strong *P* and *T* invariance in the presence of instantons," *Phys. Rev. Lett.*, vol. 40, pp. 279–282, 5 Jan. 1978.

[21] C. O'Hare, *Cajohare/axionlimits: Axionlimits*, https://cajohare.github.io/AxionLimits/, version v1.0, Jul. 2020.

[22] N. Crisosto et al., "ADMX SLIC: Results from a superconducting LC circuit investigating cold axions," *Phys. Rev. Lett.*, vol. 124, p. 241 101, 24 Jun. 2020.

Reference II

[23] R. Khatiwada, "Axion Dark Matter Experiment: Detailed design and operations," *Review of Scientific Instruments*, vol. 92, Dec. 2021.

[24] B. Majorovits and for theMADMAX interest groupt, "MADMAX: A new road to axion dark matter detection," *Journal of Physics: Conference Series*, vol. 1342, no. 1, p. 012 098, Jan. 2020.

[25] K. Barth et al., "Commissioning and first operation of the cryogenics for the CERN Axion Solar Telescope (CAST)," *AIP Conference Proceedings*, vol. 710, no. 1, pp. 168–175, Jun. 2004.

[26] I. Oceano, "Axion and ALP search with the Any Light Particle Search II experiment at DESY,", ser. 2758838, European Physical Society Conference on High Energy Physics, Hamburg (Germany), 20 Aug 2023 - 25 Aug 2023, vol. (EPS-HEP2023), Trieste: SISSA, Aug. 2023, p. 117.

[27] D. M. Pozar, *Microwave Engineering*, 4th ed. Hoboken, NJ: Wiley, 2012.

[28] M. Simanovskaia and K. van Bibber, "Status of the ADMX-HF Experiment,", ser. DESY-PROC, 11th Patras Workshop on Axions, WIMPs and WISPs, Zaragoza (Spain), 22 Jun 2015 - 26 Jun 2015, Hamburg: Verlag Deutsches Elektronen-Synchrotron, Jun. 2015, pp. 157–163.

[29] S. Youn, J. Jeong, and Y. K. Semertzidis, "Development of axion haloscopes for high-mass search at CAPP," *Frontiers in Physics*, vol. Volume 12 - 2024, Feb. 2024.

[30] J. Yang et al., "Search for 5–9 μeV axions with ADMX four-cavity array," *Springer Proc. Phys.*, vol. 245, G. Carosi and G. Rybka, Eds., pp. 53–62, Aug. 2020.

[31] T. A. Dyson et al., "High-volume tunable resonator for axion searches above 7 ghz," *Phys. Rev. Appl.*, vol. 21, p. L041002, 4 Apr. 2024.

Backup

Axion

- Solve Strong CP Problem
  - Peccei–Quinn symmetry [18]
  - Predicts a pseudoscalar Nambu–Goldstone boson
    - Weinberg [19]
    - Wilczek [20]
- Compelling CDM candidate
  - Mass range $O(1\text{–}100)\,\mu\mathrm{eV}$
  - Corresponding to MW photons
- Coupling constant $g_{a\gamma\gamma} = \left(\frac{g_\gamma \alpha}{\pi \Lambda^2}\right) m_a$
  - KSVZ: $g_\gamma = -0.97$
  - DFSZ: $g_\gamma = 0.36$

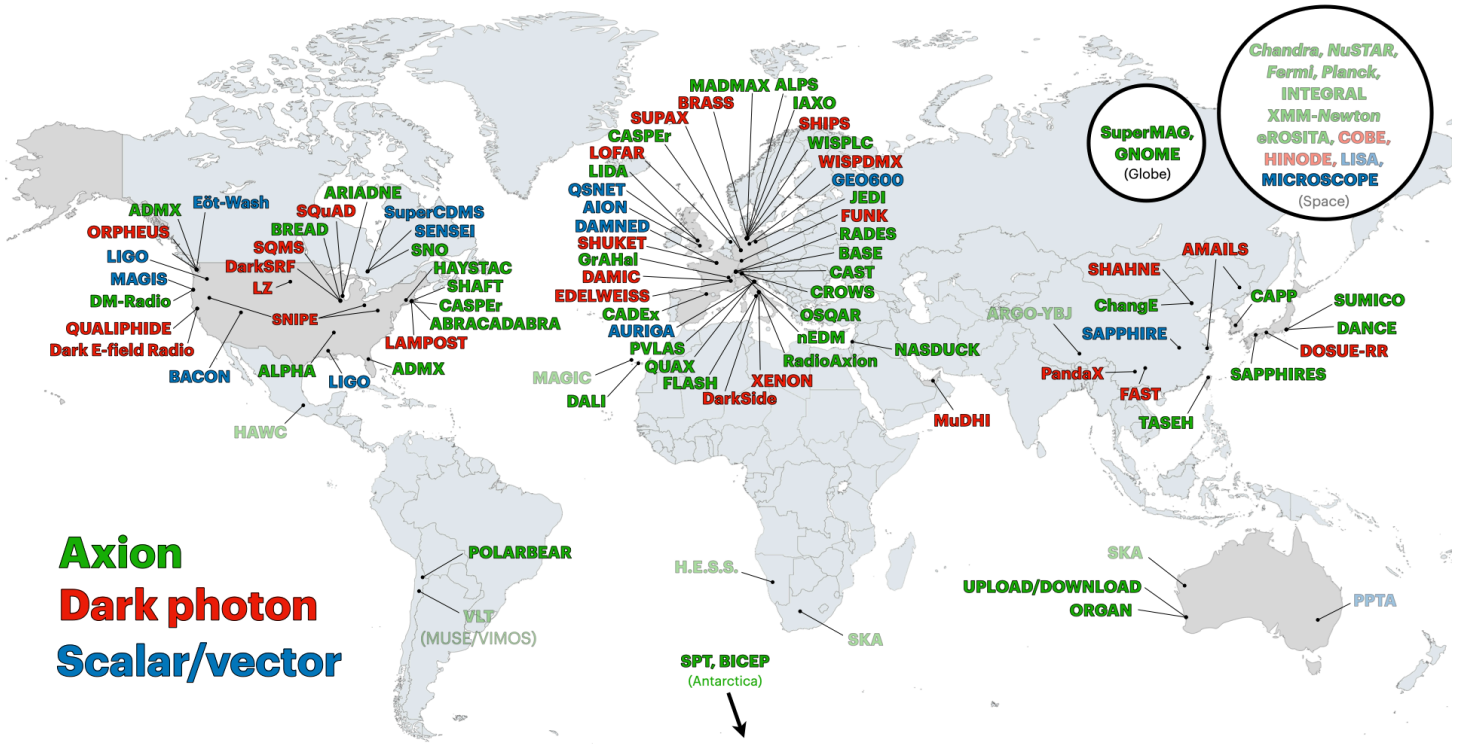


Figure 32: Worldwide Distribution of Experiments Searching for Axions, Axion-Like Particles, Dark Photons, and Other Ultralight Bosons [21].

Strong-CP problem

QCD Lagrangian

$$L_\theta = -\bar{\theta}\frac{g^2}{32\pi^2}G_a^{\mu\nu}\tilde{G}_{a\mu\nu} \tag{2}$$

θ: CP violation term

- Neutron Electrical Dipole Moment (nEDM)

  $\Rightarrow \bar{\theta} \sim 0$ in strong interaction

Axion Electrodynamics

(Heaviside–Lorentz units together with natural units are employed.)

- Lagrangian

$$L = L_{EM} + L_a + L_{g_{a\gamma\gamma}} \tag{3}$$
$$= \frac{1}{2}\left(\epsilon\vec{E}\cdot\vec{E} - \frac{1}{\mu}\vec{B}\cdot\vec{B}\right) - \rho_{\text{EM}}\Phi + \vec{J}_{\text{EM}}\cdot\vec{A} + \frac{1}{2}[(\partial_t a)^2 - (\vec{\nabla}a)^2] - \frac{1}{2}m_a^2 a^2 - g_{a\gamma\gamma}a\vec{E}\cdot\vec{B}$$

- Modified Maxwell equations

$$\begin{cases} \nabla\cdot\left(\vec{D} - g_{a\gamma\gamma}a\vec{B}\right) = \rho_{\text{EM}} & \text{— Modified Gauss's law} \quad (4a) \\ \nabla\times\left(\vec{H} + g_{a\gamma\gamma}a\vec{E}\right) - \frac{\partial}{\partial t}\left(\vec{D} - g_{a\gamma\gamma}a\vec{B}\right) = \vec{J}_{\text{EM}} & \text{— Modified Ampère-Maxwell law} \quad (4b) \\ \nabla\cdot\vec{B} = 0 & (4c) \\ \nabla\times\vec{E} + \frac{\partial\vec{B}}{\partial t} = 0 & (4d) \end{cases}$$

- Axion field equation

$$\partial_t^2 a - \nabla^2 a + m_a^2 a = -g_{a\gamma\gamma}\vec{E}\cdot\vec{B} \quad \text{— Axion equation (inhomogeneous K-G)} \tag{5}$$

⇒ The axion field induces an effective electric charge $\rho_a = -g_{a\gamma\gamma}\vec{B}\cdot\nabla a$

and an effective current density $\vec{J}_a = -g_{a\gamma\gamma}\left(\frac{\partial a}{\partial t}\vec{B} + \nabla a\times\vec{E}\right)$

⇒ CDM: non-relativistic axions, $|\partial_t a| \gg |\nabla a| \Rightarrow \nabla a \simeq 0 \Rightarrow \vec{J}_a = -g_{a\gamma\gamma}\frac{\partial a}{\partial t}\vec{B}$

Lagrangian & Action

- Total Lagrangian density: $L = L_{EM} + L_a + L_{g_{a\gamma\gamma}}$
  - $L_{EM} = \frac{1}{2}\left(\epsilon\vec{E}\cdot\vec{E} - \frac{1}{\mu}\vec{B}\cdot\vec{B}\right) - \rho_{\text{EM}}\Phi + \vec{J}_{\text{EM}}\cdot\vec{A}$
  - $L_a = \frac{1}{2}\left[(\partial_t a)^2 - (\vec{\nabla}a)^2\right] - \frac{1}{2}m_a^2 a^2$
  - $L_{g_{a\gamma\gamma}} = -g_{a\gamma\gamma}\, a\vec{E}\cdot\vec{B}$
- Action: $S = \int L\, d^3x\, dt$
  - Principle of stationary action: $\delta S = 0$
  - $\delta S_\Phi = 0 \Rightarrow$ **Modified Gauss's law**
  - $\delta S_{\vec{A}} = 0 \Rightarrow$ **Modified Ampère-Maxwell law**
  - $\delta S_a = 0 \Rightarrow$ **Axion equation (inhomogeneous K-G)**

Variation w.r.t. Scalar Potential Φ

1. Extract Φ-dependent terms

$$L_\Phi = \frac{1}{2}\epsilon\vec{E}\cdot\vec{E} - \rho_{\text{EM}}\Phi - g_{a\gamma\gamma}\, a\vec{E}\cdot\vec{B}$$

2. Apply $\delta\Phi$, use $\delta\vec{E} = -\vec{\nabla}(\delta\Phi)$

$$\delta S_\Phi = \int \left[-(\epsilon\vec{E} - g_{a\gamma\gamma} a\vec{B})\cdot\vec{\nabla}(\delta\Phi) - \rho_{\text{EM}}\,\delta\Phi\right] d^3x\, dt$$

3. Integration by parts + divergence theorem
   - Vector identity: $\vec{F}\cdot\vec{\nabla}(\delta\Phi) = \vec{\nabla}\cdot(\vec{F}\,\delta\Phi) - (\vec{\nabla}\cdot\vec{F})\,\delta\Phi$
   - Surface term vanishes: $\delta\Phi|_{\partial V} = 0$

$$\delta S_\Phi = \int \left[\vec{\nabla}\cdot(\epsilon\vec{E} - g_{a\gamma\gamma} a\vec{B}) - \rho_{\text{EM}}\right]\delta\Phi\; d^3x\, dt$$

4. $\delta S_\Phi = 0$ for arbitrary $\delta\Phi$

Modified Gauss's law

$$\vec{\nabla}\cdot(\epsilon\vec{E} - g_{a\gamma\gamma}\, a\,\vec{B}) = \rho_{\text{EM}}$$

Variation w.r.t. Vector Potential $\vec{A}$

1. Extract $\vec{A}$-dependent terms

$$L_{\vec{A}} = \frac{\epsilon}{2}\vec{E}\cdot\vec{E} - \frac{1}{2\mu}\vec{B}\cdot\vec{B} + \vec{J}_{\text{EM}}\cdot\vec{A} - g_{a\gamma\gamma}a\vec{E}\cdot\vec{B}$$

2. Apply $\delta\vec{A}$: $\delta\vec{E} = -\partial_t(\delta\vec{A})$, $\quad \delta\vec{B} = \vec{\nabla}\times(\delta\vec{A})$

3. Integration by parts (temporal + spatial)
   - Temporal: $\int \vec{F}\cdot\partial_t(\delta\vec{A})\,dt = -\int \partial_t\vec{F}\cdot\delta\vec{A}\,dt$
   - Spatial: $\int \vec{F}\cdot(\vec{\nabla}\times\delta\vec{A})\,d^3x = \int(\vec{\nabla}\times\vec{F})\cdot\delta\vec{A}\,d^3x$

$$\delta S_{\vec{A}} = \int\left[\partial_t(\epsilon\vec{E} - g_{a\gamma\gamma}a\vec{B}) - \vec{\nabla}\times\left(\frac{1}{\mu}\vec{B} + g_{a\gamma\gamma}a\vec{E}\right) + \vec{J}_{\text{EM}}\right]\cdot\delta\vec{A}\,d^3x\,dt$$

4. $\delta S_{\vec{A}} = 0$ for arbitrary $\delta\vec{A}$

Modified Ampère-Maxwell law

$$\vec{\nabla}\times\left(\frac{1}{\mu}\vec{B} + g_{a\gamma\gamma}a\vec{E}\right) - \partial_t(\epsilon\vec{E} - g_{a\gamma\gamma}a\vec{B}) = \vec{J}_{\text{EM}}$$

Variation w.r.t. Axion Field a

1. Extract a-dependent terms

$$L_a = \underbrace{\frac{1}{2}(\partial_t a)^2 - \frac{1}{2}(\vec{\nabla} a)^2 - \frac{1}{2} m_a^2 a^2}_{\text{Klein-Gordon Lagrangian}} - g_{a\gamma\gamma}\, a \vec{E} \cdot \vec{B}$$

2. Apply $a \to a + \delta a$

$$\delta S_a = \int \left[\partial_t a \cdot \partial_t(\delta a) - \vec{\nabla} a \cdot \vec{\nabla}(\delta a) - m_a^2 a\, \delta a - g_{a\gamma\gamma} \vec{E} \cdot \vec{B}\, \delta a \right] d^3x\, dt$$

3. Integration by parts
   - Temporal: $\int \partial_t a \cdot \partial_t(\delta a)\, dt = -\int \partial_t^2 a \cdot \delta a\, dt$
   - Spatial: $-\int \vec{\nabla} a \cdot \vec{\nabla}(\delta a)\, d^3x = \int \nabla^2 a \cdot \delta a\, d^3x$

$$\delta S_a = \int \left[-\partial_t^2 a + \nabla^2 a - m_a^2 a - g_{a\gamma\gamma} \vec{E} \cdot \vec{B} \right] \delta a\, d^3x\, dt$$

4. $\delta S_a = 0$ for arbitrary δa

Axion equation (inhomogeneous K-G)

$$\partial_t^2 a - \nabla^2 a + m_a^2 a = -g_{a\gamma\gamma} \vec{E} \cdot \vec{B}$$

Axion Detection

- Haloscope (Fig. 34(a)–(c))
  - Galactic DM axions
  - The most sensitive method
- Helioscope (Fig. 34d)
  - Solar axions
- Light-shining-through-a-wall (Fig. 34e)
  - Pure laboratory experiment

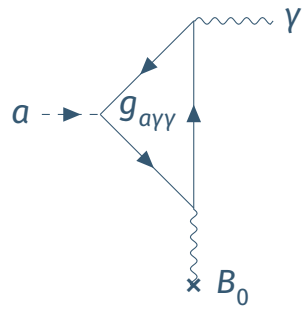
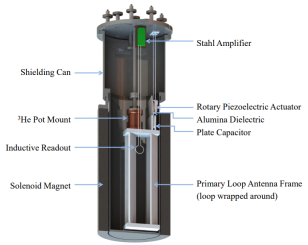
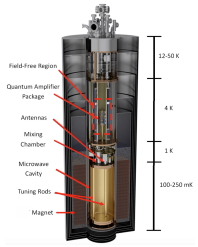


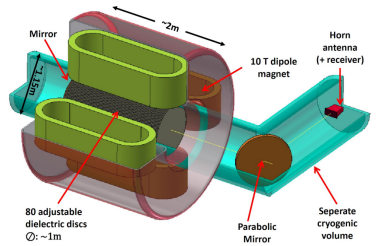
Figure 33: Inverse Primakoff effect



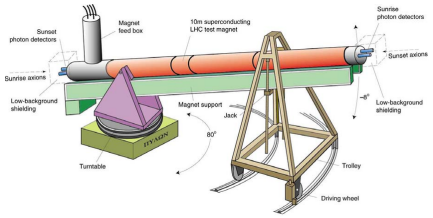
(a) Haloscope - Lumped circuit ADMX SLIC [22]



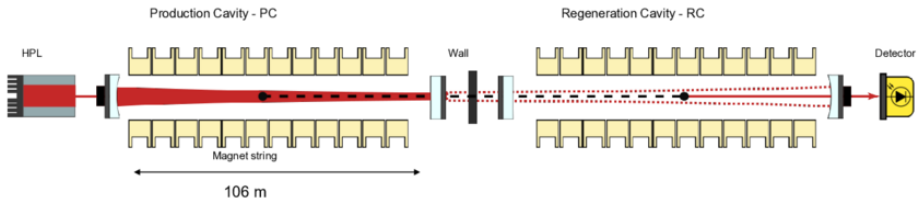
(b) Haloscope - Cavity ADMX [23]



(c) Haloscope - Dielectric disks MADMAX [24]



(d) Helioscope CAST [25]



(e) LSW ALPS II [26]

Figure 34: Schematics of representative axion detection approaches.

Axion Exclusion Plot

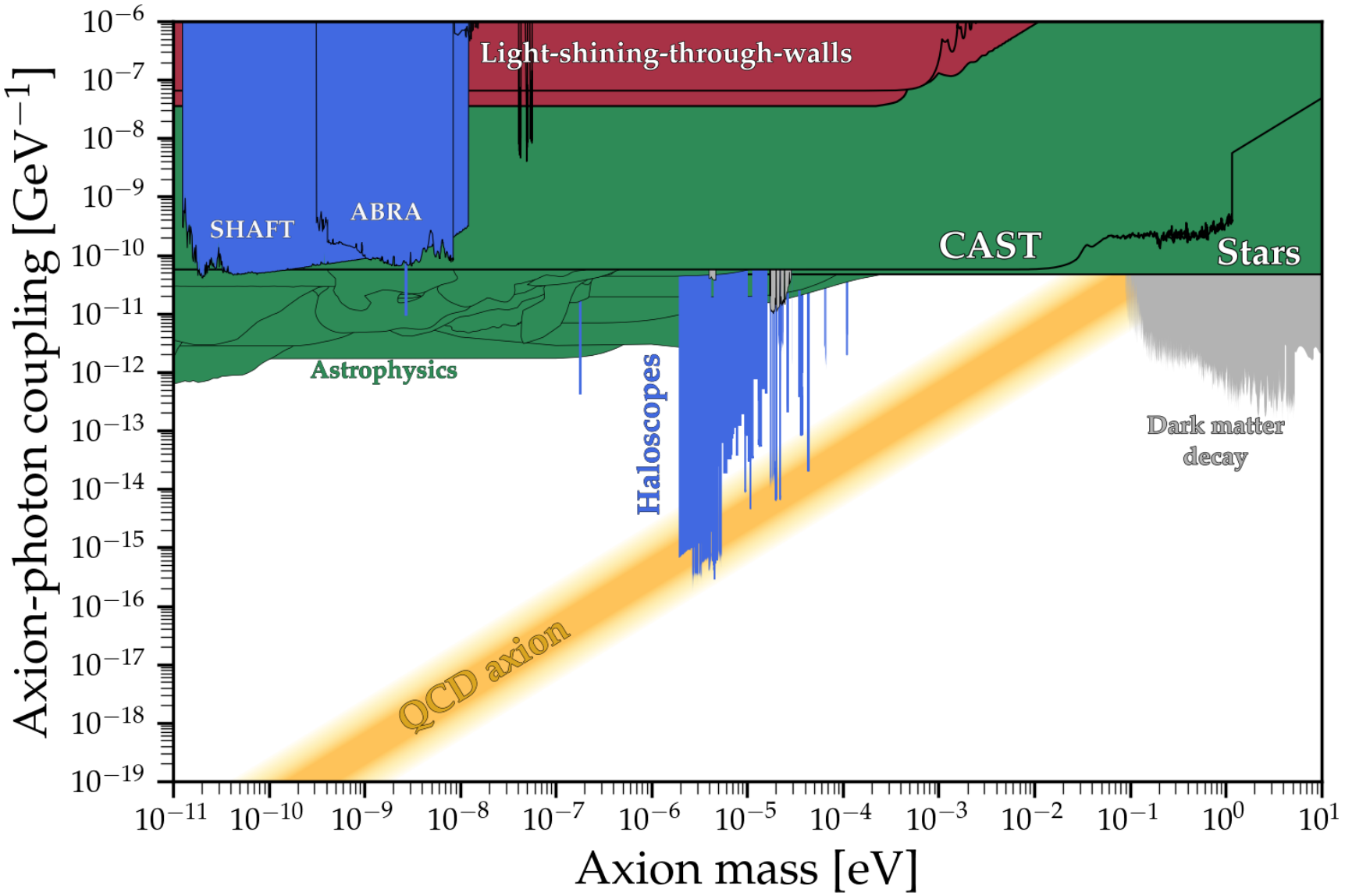


Figure 35: Axion Exclusion Plot [21]. Green: helioscope experiments and astronomical observations; Red: LSW experiments; Blue: haloscope experiments. Yellow: QCD axion band.

Axion Exclusion Plot - Haloscope

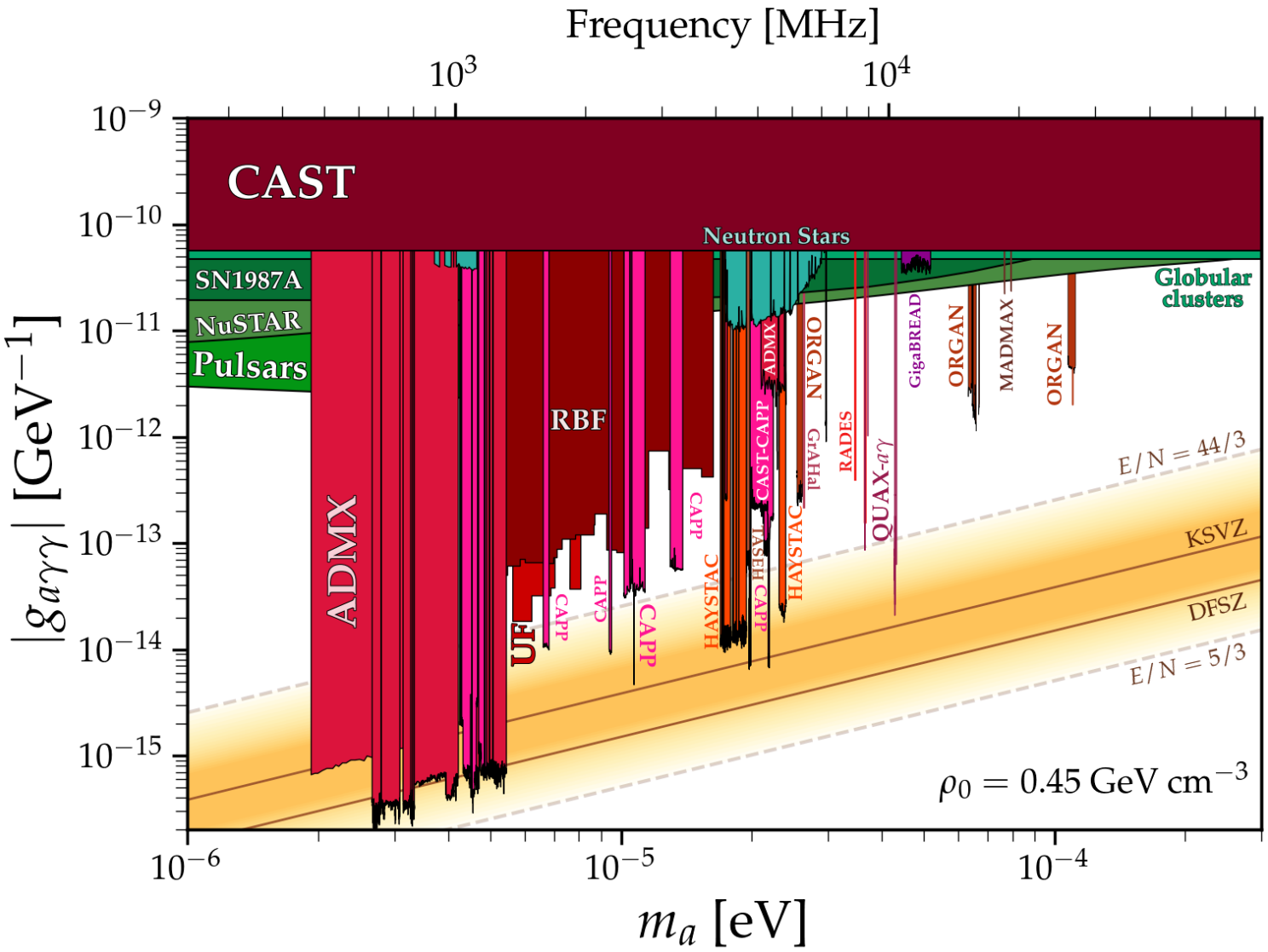


Figure 36: Close-Up View of the Haloscope Axion Exclusion Plot [21].

TASEH

CD102 [1], [2], [3]

- $g_{a\gamma\gamma}$ ~11x KSVZ
- f_r :4.7075–4.79815 GHz (19.47–19.76 μeV)
- Cavity 0.234L
- HEMT Amplifier
- Magnet 8T

CDT045

- $g_{a\gamma\gamma}$ ~3x KSVZ
- f_r :2.156–2.180 GHz (8.91–9.01 μeV)
- Cavity 4.1L
- JPA
- Magnet 6T (9T is preparing)

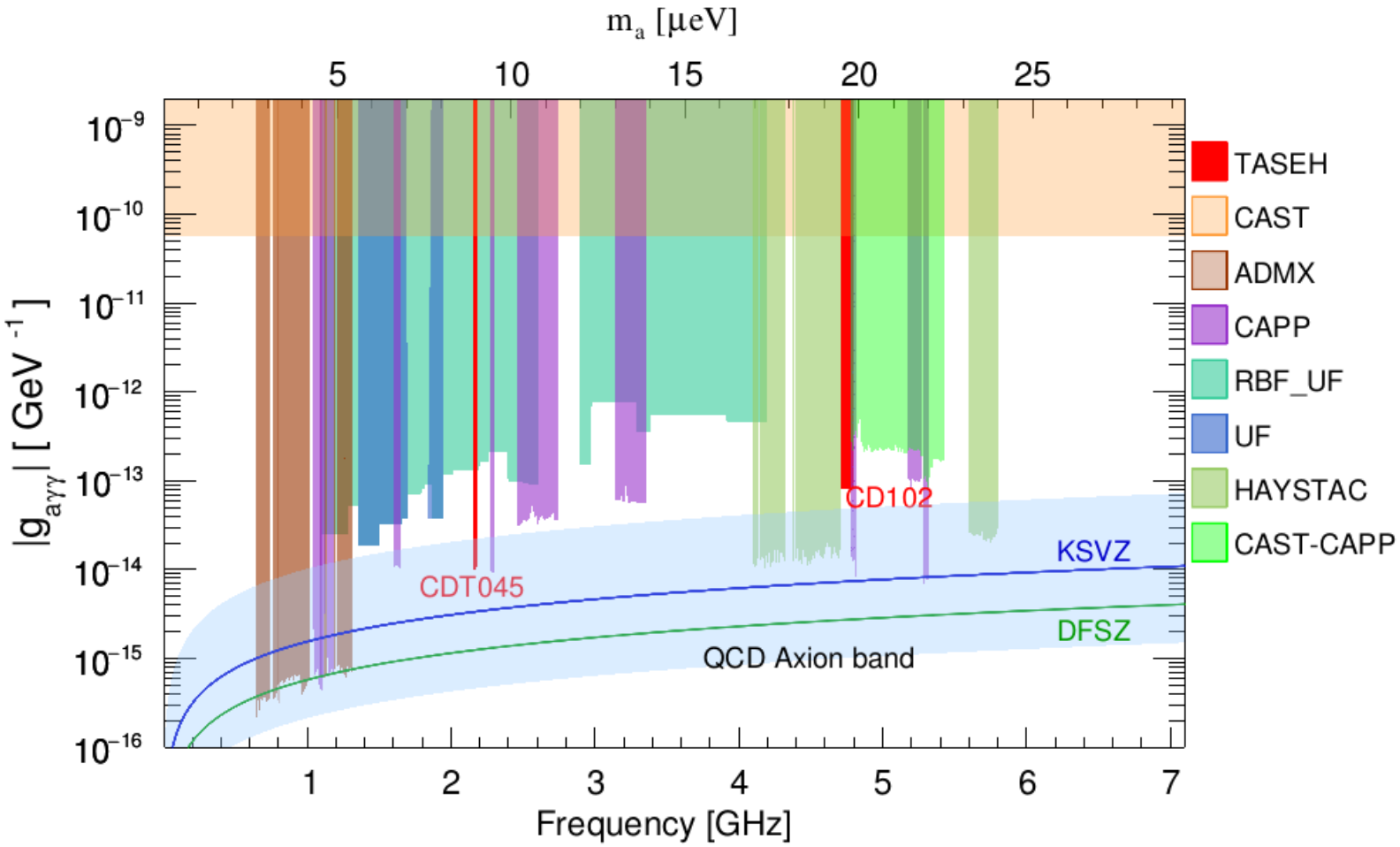


Figure 37: Axion Exclusion Plot [3].

Signal Extraction

- Signal Power (SI units)

$$P_s = g_{a\gamma\gamma}^2 \frac{\hbar^3 c^3 \rho_a}{m_a^2} \omega_r \frac{1}{\mu_0} B_0^2 V C Q_0 \frac{\beta}{(1+\beta)^2} \tag{6}$$

- System Noise

$$\sigma_n = k_B T_{sys} \sqrt{\frac{\Delta f}{t}} \tag{7}$$

- Signal-to-Noise Ratio

$$SNR = \frac{P_s}{\sigma_n} \tag{8}$$

- Step Size

$$df = \frac{1}{2}\frac{f_r}{Q_L} = \frac{f_r(1+\beta)}{2Q_0} \tag{9}$$

- Scan Rate

$$\frac{df}{dt} \propto \frac{g_{a\gamma\gamma}^4 B_0^4 C^2 V^2 Q_0 \beta^2}{k_B^2 T_{sys}^2 (1+\beta)^3} \tag{10}$$

- Figure of Merit (FoM)

$$\frac{1}{g_{a\gamma\gamma}} \propto B_0 \sqrt{\frac{CV\sqrt{Q_0}}{T_{sys}}} \quad \Rightarrow \quad \text{FoM} \propto \sqrt{CV\sqrt{Q_0}} \tag{11}$$

C: form factor V: volume Q_0: Intrinsic quality factor

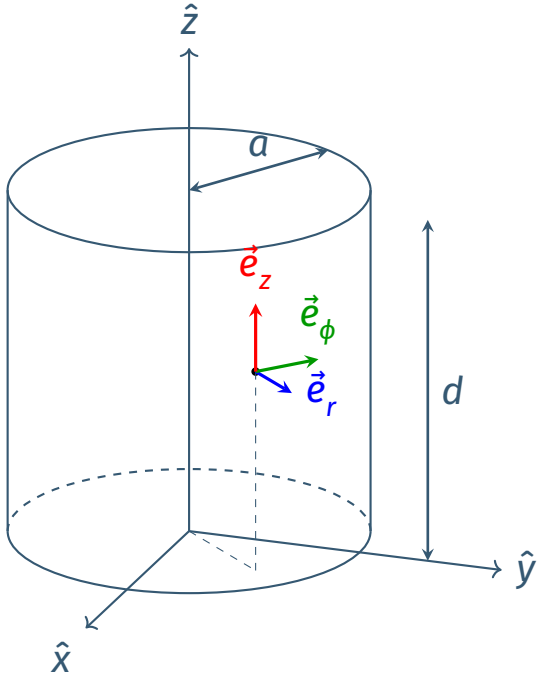


Figure 38: Cylindrical Cavity.

- TM mode resonant frequency for cylindrical cavity [27]

$$f_{nml} = \frac{c}{2\pi\sqrt{\mu_r \epsilon_r}} \sqrt{\left(\frac{P_{nm}}{a}\right)^2 + \left(\frac{l\pi}{d}\right)^2} \tag{12}$$

  - P_{nm}: m^{th} root of $J_n(x) = 0$
  - TM_{010} mode is prefered.

HF large-volume cavity design:

- Upsize Rods & Radius (Fig. 39)
- Multi-cell / Periodic Structures (Fig. 40)
- Multi-cavity Configurations (Fig. 41)
- Advanced Geometries (Fig. 42)

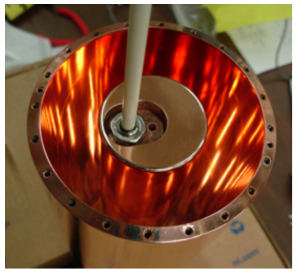


Figure 39: ADMX-HF [28]

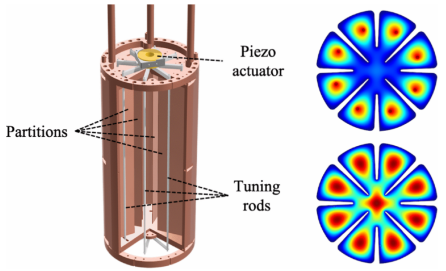


Figure 40: CAPP 8Cell [29]

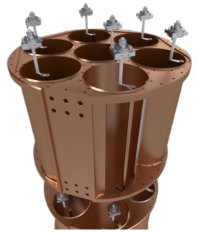


Figure 41: ADMX-G2 [30]

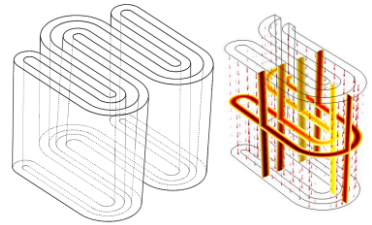


Figure 42: Thin shell [31]

Form factor C

- = Geometry factor G

$$C = \frac{\left[\int (\vec{B} \cdot \vec{E})\, dV\right]^2}{B_0^2 V \int |\vec{E}|^2\, dV} \tag{13}$$

E: Electric field of selected mode. B: Magnetic field of external magnet.

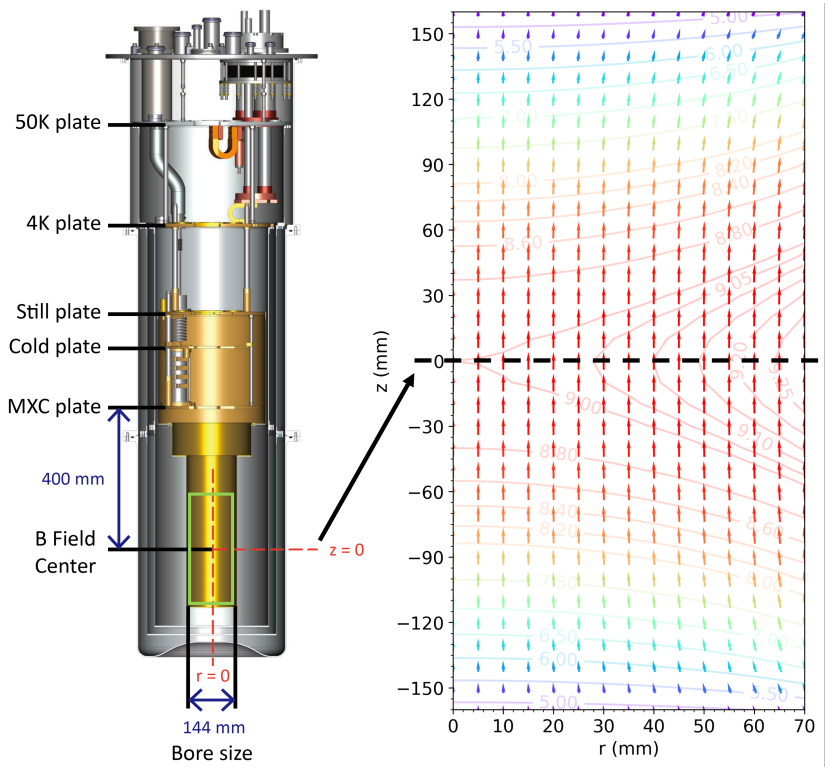


Figure 43: DR & B field

- Mode Interaction

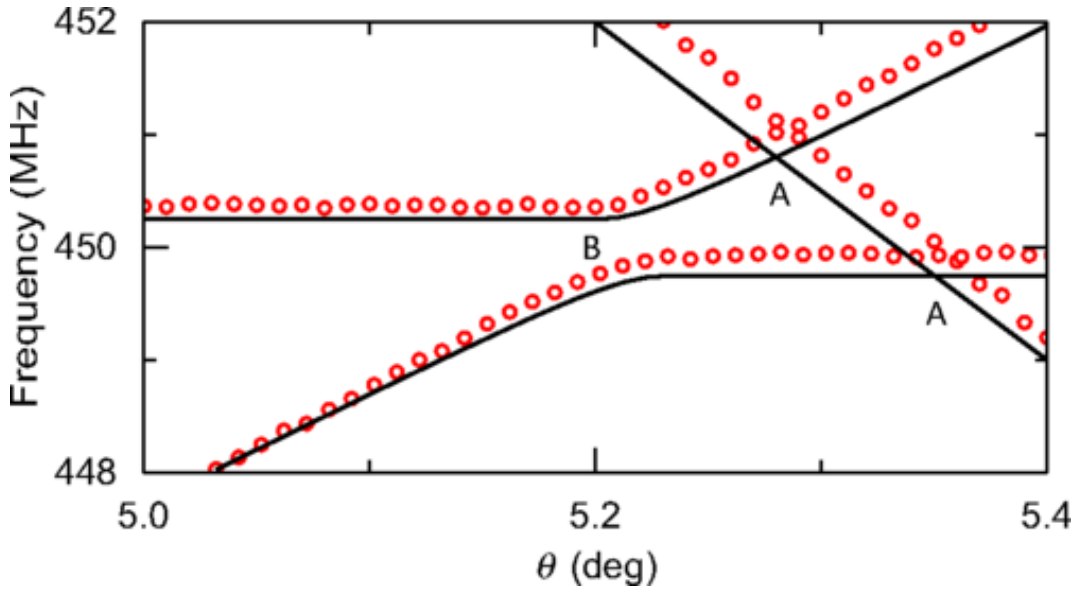


Figure 44: Mode interaction [28]

Slater Bead Perturbation Theory

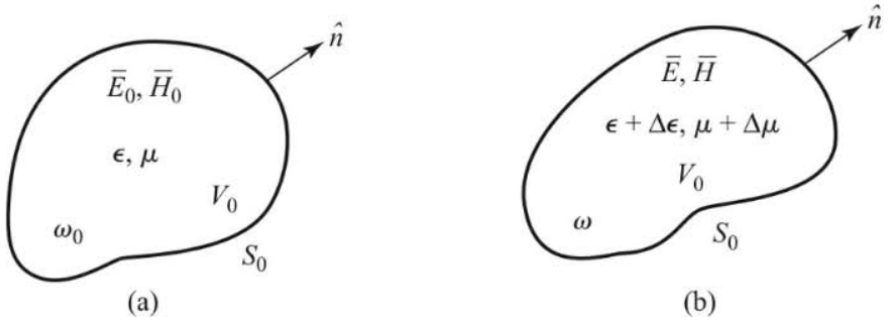
1. Original vs. Perturbed Cavity
   - Original:

     $\nabla \times \vec{E}_0 = -j\omega_0 \mu \vec{H}_0$

     $\nabla \times \vec{H}_0 = j\omega_0 \epsilon \vec{E}_0$
   - Perturbed:

     $\nabla \times \vec{E} = -j\omega(\mu + \Delta\mu)\vec{H}$

     $\nabla \times \vec{H} = j\omega(\epsilon + \Delta\epsilon)\vec{E}$



2. Cross-multiply + vector identity: $\nabla \cdot (\vec{A} \times \vec{B}) = \vec{B} \cdot (\nabla \times \vec{A}) - \vec{A} \cdot (\nabla \times \vec{B})$
3. Integrate over V_0 + divergence theorem

$$\Rightarrow \frac{\omega - \omega_0}{\omega} = \frac{-\int_{V_0} (\Delta\epsilon\, \vec{E}_0^* \cdot \vec{E} + \Delta\mu\, \vec{H}_0^* \cdot \vec{H})\, dv}{\int_{V_0} (\epsilon\, \vec{E}_0^* \cdot \vec{E} + \mu\, \vec{H}_0^* \cdot \vec{H})\, dv}$$

4. Small perturbation: $\vec{E} \approx \vec{E}_0$, $\vec{H} \approx \vec{H}_0$, $\omega \approx \omega_0$

Slater Perturbation Theorem

$$\frac{\Delta\omega}{\omega_0} \cong \frac{-\int_{V_0} (\Delta\epsilon |\vec{E}_0|^2 + \Delta\mu |\vec{H}_0|^2)\, dv}{\int_{V_0} (\epsilon |\vec{E}_0|^2 + \mu |\vec{H}_0|^2)\, dv}$$

5. For dielectric bead ($\Delta\mu = 0$): $\Delta f \propto |\vec{E}_0|^2$ at bead location

Intrinsic quality factor Q_0

- Quality Factor

$$Q = \omega_r \frac{U}{P} = \frac{f_r}{\Delta f} = \frac{\omega_r}{\Delta \omega} = \omega_r \kappa \qquad (14)$$

  - Intrinsic Q: Q_i, Q_0
  - External Q: Q_e, Q_c
  - Loaded Q: Q_L

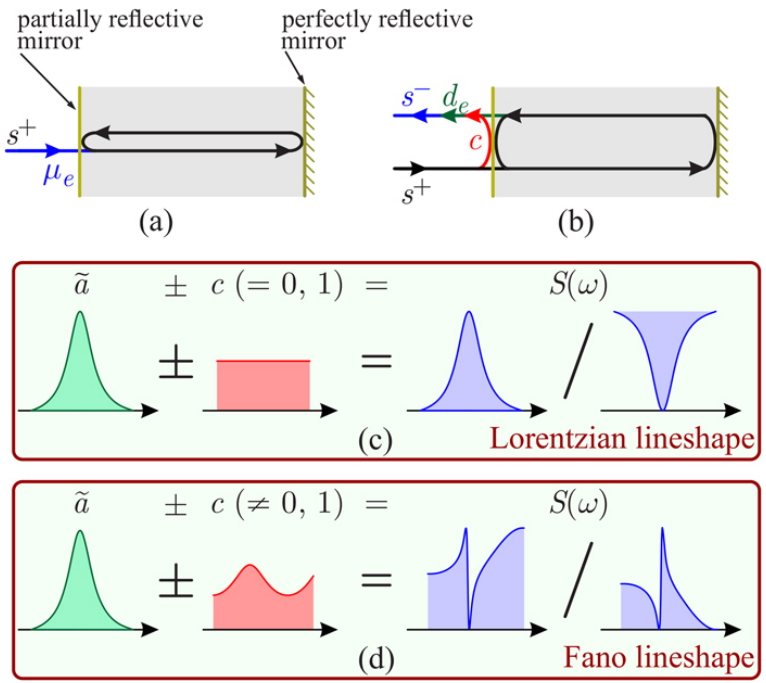


Figure 45: Coupling schematic of the microwave cavity and the output scattering line shape.

- Key Factors
  - Material
    - High RRR
  - Structure

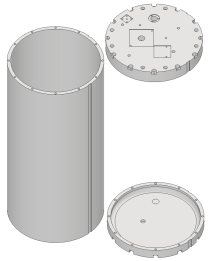


Figure 46: 3-section

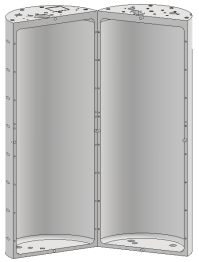


Figure 47: Split

- Low T & High B environment
  - Skin depth
    - Anomalous skin depth (ASE)

$$\delta_a = \sqrt[3]{\frac{\sqrt{3}\, c^2 m_e v_F}{8\pi\omega n e^2}}$$

  - Electron mean free path
  - Cyclotron radius

⇒ Non-monotonic Q_0(B, T)

Equivalent Circuit

Quality Factor

$$Q = \omega_r \frac{U}{P} = \frac{f_r}{\Delta f} = \frac{\omega_r}{\Delta \omega} = \omega_r \kappa \tag{15}$$

- Intrinsic Q Q_i, Q_0

$$Q_i = \omega_r \frac{L}{R} \tag{16}$$

- External Q Q_e, Q_c

$$Q_e = \omega_r \frac{L}{Z_0} = \frac{Q_i}{\beta} \tag{17}$$

- Loaded Q Q_L

$$Q_L = \omega_r \frac{L}{R + Z_0} = \frac{Q_i}{1 + \beta} \tag{18}$$

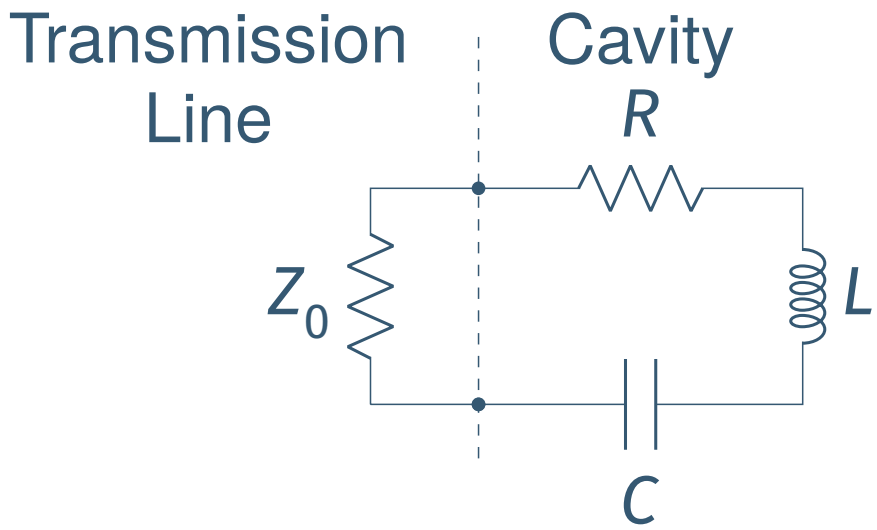


Figure 48: Equivalent Circuit.

Coupling coefficient β

- Coupling Coefficient β

$$\beta = \frac{Q_i}{Q_e} = \frac{\kappa_e}{\kappa_i} \tag{19}$$

- $\frac{df}{dt} \propto \frac{\beta^2}{(1+\beta)^3} \quad \Rightarrow \frac{d}{d\beta}\frac{\beta^2}{(1+\beta)^3} = 0 \quad \Rightarrow \beta = 2$

Table 4: Experimental parameters versus the coupling coefficient β

β	0.5	1	1.5	2	2.5	3	
$\frac{\beta}{(1+\beta)^2}$	0.2222	0.2500	0.2400	0.2222	0.2041	0.1875	$\propto P_s$
$\frac{\beta^2}{(1+\beta)^3}$	0.0741	0.1250	0.1440	0.1481	0.1458	0.1406	$\propto \frac{df}{dt}$
$\frac{(1+\beta)^{\frac{3}{4}}}{\beta^{\frac{1}{2}}}$	0.5217	0.5946	0.6160	0.6204	0.6179	0.6124	$\propto g_{a\gamma\gamma}$
$\frac{g_{a\gamma\gamma}(\beta)}{g_{a\gamma\gamma}(\beta=2)}$	0.8409	0.9584	0.9929	1.0000	0.9960	0.9871	

Perturbative Solution for Conic Geometry

- Setup: tilted PEC walls
  - $R_i(z) = r_i - z\tan\theta_i, \quad \hat{n}_i \propto \hat{r} + \tan\theta_i\,\hat{z}$
  - B.C.: $\hat{n} \times \vec{E} = 0 \Rightarrow E_z = E_r \tan\theta_i$ at $r = R_i(z)$
  - Expansion: $E_z = E_z^{(0)} + E_z^{(1)} + E_z^{(2)}, \;\; k_c^2 = k_c^{(0)2} + 2k_c^{(0)}k_c^{(1)} + k_c^{(1)2} + 2k_c^{(0)}k_c^{(2)}$
- Field correction (Taylor expansion + B.C. matching)

$$E_z^{(1)}(r_i, z) = -k_c^{(0)}\, z \tan\theta_i\, \Psi_1(k_c^{(0)} r_i)$$

$$E_z^{(2)}(r_i, z) = \frac{k_c^{(0)}}{2r_i} E_r^{(1)} \tan\theta_i + z^2 \tan^2\theta_i\, \Psi_1(k_c^{(0)} r_i)$$

($E_r^{(0)} = 0$ in TM_{010}; geometric coupling enters only at 2nd order)

- Frequency correction (Helmholtz $(\nabla_T^2 + k_c^2)E_z = 0$)

Frequency Corrections

$$k_c^{(1)} = k_c^{(0)} \frac{[r\tan\theta_i\,\Psi_1^2]_{r_2}^{r_1}}{[r^2\Psi_1^2]_{r_2}^{r_1}}$$

C Decomposition & V Correction

- Form factor decomposition: $N = \int E_z \, dV, \quad P = \int |E_z|^2 \, dV$

$$C = \frac{N^2}{VP}$$

- Expand to 2nd order (with $N_n \equiv N^{(n)}/N_0$, etc.; $P_1 = 0$ by orthogonality)

Form Factor (2nd-order expansion)

$$C_{\text{conic}} \approx C_{\text{coax}} \left(1 + 2N_1 + 2N_2 + N_1^2\right)\left[1 - (V_1 + V_2) + V_1^2\right]\left[1 - P_2\right]$$

- Volume correction (exact, $V_{\text{conic}} = \pi \int_0^d [R_1^2(z) - R_2^2(z)]\, dz$)

$$V_{\text{conic}} = \underbrace{\pi d (r_1^2 - r_2^2)}_{V_0} - \underbrace{\pi d^2 (r_1 \tan\theta_1 - r_2 \tan\theta_2)}_{V^{(1)}} + \underbrace{\frac{\pi d^3}{3}(\tan^2\theta_1 - \tan^2\theta_2)}_{V^{(2)}}$$

- At design point: $V_1 < 0 \Longrightarrow$ field concentrates $\Longrightarrow C \uparrow$

N & *P* Correction Highlights

- *N* correction —1st order:

$$N_1 = -\frac{d}{2}\frac{k_c^{(1)}}{k_c^{(0)}} \sim O(10^{-3})$$

- *N* correction —2nd order (3 contributions): $N^{(2)} = A + B + C$
  - *A*: 2nd-order field

$$A = \frac{2\pi d^3}{3k_c^{(0)}}\left[\frac{k_c^{(1)2}}{6}\frac{[r^4\Psi_1^2(k_c^{(0)}r)]_{r_2}^{r_1}}{[r^2\Psi_1^2(k_c^{(0)}r)]_{r_2}^{r_1}} + \frac{k_c^{(1)}}{k_c^{(0)2}}\left(k_c^{(1)} + \frac{11}{3}\right)[r\Psi_1(k_c^{(0)}r)]_{r_2}^{r_1} - \frac{k_c^{(1)}}{2}[r^3\Psi_1(k_c^{(0)}r)]_{r_2}^{r_1}\right]$$

  - *B*: 1st-order field × 1st-order B.C.
  - *C*: zero-order field × 2nd-order B.C.
  - **Geometric contribution** *B*+*C*: $\frac{\pi d^3}{3}k_c^{(0)}[r\tan^2\theta_i\,\Psi_1]_{r_2}^{r_1}$
- *P* correction:
  - $P_1 = 0$ (orthogonality: $\int E_z^{(0)}E_z^{(1)}\,dV = 0$)
  - $P_2 = \frac{2d^2}{3}\left(\frac{k_c^{(1)}}{k_c^{(0)}}\right)^2\left[1 - \frac{1}{3k_c^{(0)2}} + \frac{[r^4\Psi_1^2]_{r_2}^{r_1}}{6[r^2\Psi_1^2]_{r_2}^{r_1}}\right] \sim O(10^{-5})$

Complete Correction Table

Go Back

Term	Order	Expression
$k_c^{(1)}$	$O(\alpha)$	$k_c^{(0)} \dfrac{\left[r \tan\theta_i \, \psi_1^2(k_c^{(0)} r)\right]_{r_2}^{r_1}}{\left[r^2 \psi_1^2(k_c^{(0)} r)\right]_{r_2}^{r_1}}$
$k_c^{(2)}$	$O(\alpha^2)$	$\dfrac{3}{2}\dfrac{k_c^{(1)2}}{k_c^{(0)}} + \dfrac{k_c^{(1)}\left[r \tan\theta_i \, \psi_1^2(k_c^{(0)} r)\right]_{r_2}^{r_1}}{\left[r^2 \psi_1^2(k_c^{(0)} r)\right]_{r_2}^{r_1}} + \dfrac{k_c^{(0)}\left[\tan^2\theta_i \, \psi_1^2(k_c^{(0)} r)\right]_{r_2}^{r_1}}{2\left[r^2 \psi_1^2(k_c^{(0)} r)\right]_{r_2}^{r_1}}$
N_0	$O(1)$	$\dfrac{2\pi d}{k_c^{(0)}}\left[r\psi_1(k_c^{(0)} r)\right]_{r_2}^{r_1}$
N_1	$O(\alpha)$	$-\dfrac{d}{2}\dfrac{k_c^{(1)}}{k_c^{(0)}}$
N_2	$O(\alpha^2)$	$\dfrac{d^2}{3k_c^{(0)}}\left\{\dfrac{k_c^{(1)2}}{6}\dfrac{\left[r^4\psi_1^2\right]_{r_2}^{r_1}}{\left[r^2\psi_1^2\right]_{r_2}^{r_1}} + \dfrac{k_c^{(1)}}{k_c^{(0)2}}\left(k_c^{(1)} + \dfrac{11}{3}\right) - \dfrac{k_c^{(1)}}{2}\dfrac{\left[r^3\psi_1\right]_{r_2}^{r_1}}{\left[r\psi_1\right]_{r_2}^{r_1}} + \dfrac{k_c^{(0)2}}{2}\dfrac{\left[r\tan^2\theta_i \, \psi_1\right]_{r_2}^{r_1}}{\left[r\psi_1\right]_{r_2}^{r_1}}\right\}$
V_0	$O(1)$	$\pi d \left[r^2\right]_{r_2}^{r_1}$
V_1	$O(\alpha)$	$-\dfrac{d\left[r\tan\theta_i\right]_{r_2}^{r_1}}{\left[r^2\right]_{r_2}^{r_1}}$
V_2	$O(\alpha^2)$	$\dfrac{d^2}{3}\dfrac{\left[\tan^2\theta_i\right]_{r_2}^{r_1}}{\left[r^2\right]_{r_2}^{r_1}}$
P_0	$O(1)$	$\pi d\left[r^2\psi_1^2(k_c^{(0)} r)\right]_{r_2}^{r_1}$
P_1	$O(\alpha)$	0
P_2	$O(\alpha^2)$	$\dfrac{2d^2}{3}\left(\dfrac{k_c^{(1)}}{k_c^{(0)}}\right)^2\left[1 - \dfrac{1}{3k_c^{(0)2}} + \dfrac{\left[r^4\psi_1^2\right]_{r_2}^{r_1}}{6\left[r^2\psi_1^2\right]_{r_2}^{r_1}}\right]$
C_{conic}	$O(\alpha^2)$	$C_{\text{coaxial}}(1 + 2N_1 + 2N_2 + N_1^2)[1 - (V_1 + V_2) + V_1^2][1 - P_2]$